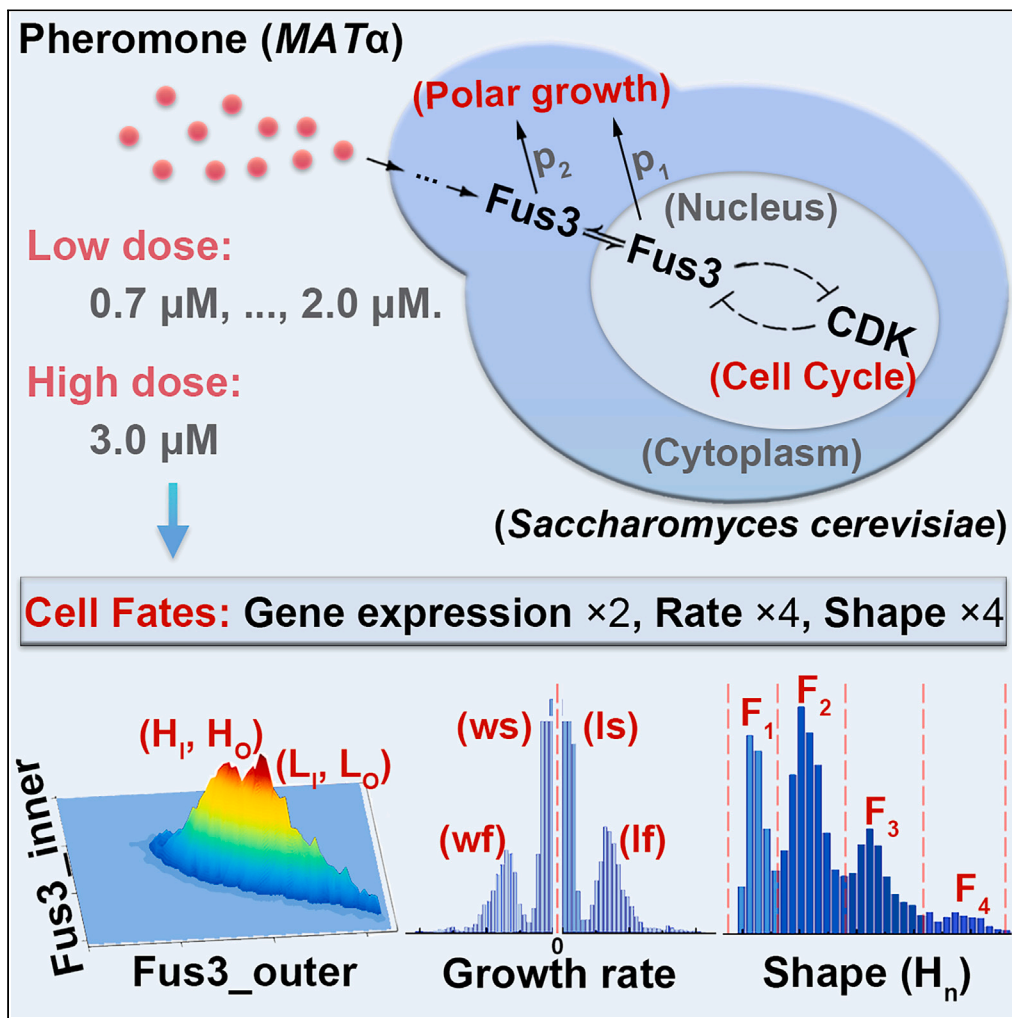


Article

Global quantitative understanding of non-equilibrium cell fate decision-making in response to pheromone



Sheng Li, Qiong Liu, Erkang Wang, Jin Wang

liuqiong@ciac.ac.cn (Q.L.)  
jin.wang.1@stonybrook.edu (J.W.)

**Highlights**

Revealed pheromone-driven non-equilibrium landscapes in cell fate decision-making

Identified diverse cell fates: Fus3 expression, growth rates, and morphologies

Validated the signaling model experimentally, confirming proposed fate mechanisms



## Article

## Global quantitative understanding of non-equilibrium cell fate decision-making in response to pheromone

Sheng Li,<sup>1,2</sup> Qiong Liu,<sup>2,\*</sup> Erkang Wang,<sup>1,2</sup> and Jin Wang<sup>3,4,\*</sup>

## SUMMARY

Cell-cycle arrest and polarized growth are commonly used to characterize the response of yeast to pheromone. However, the quantitative decision-making processes underlying time-dependent changes in cell fate remain unclear. In this study, we conducted single-cell level experiments to observe multidimensional responses, uncovering diverse fates of yeast cells. Multiple states are revealed, along with the kinetic switching rates and pathways among them, giving rise to a quantitative landscape of mating response. To quantify the experimentally observed cell fates, we developed a theoretical framework based on non-equilibrium landscape and flux theory. Additionally, we performed stochastic simulations of biochemical reactions to elucidate signal transduction and cell growth. Notably, our experimental findings have provided the first global quantitative evidence of the real-time synchronization between intracellular signaling, physiological growth, and morphological functions. These results validate the proposed underlying mechanism governing the emergence of multiple cell fate states. This study introduces an emerging mechanistic approach to understand non-equilibrium cell fate decision-making in response to pheromone.

## INTRODUCTION

Facing a variety of external stimuli, cells integrate information from various sources and initiate appropriate stress responses, such as survival or death, division or differentiation, and shape change or migration.<sup>1–7</sup> To better understand the cellular response to external stimuli, we chose the pheromone pathway of *Saccharomyces cerevisiae*, which is a classical model of the mitogen-activated protein kinase (MAPK) signaling pathway.<sup>8–11</sup> *S. cerevisiae* has two modes of reproduction, sexual mating reproduction and asexual budding reproduction.<sup>12–16</sup> These two reproductive modes can be converted either with or without the assistance of external pheromone stimulation from a partner.<sup>17</sup> For sexual reproduction, mating to form a diploid cell is the natural behavior of heterothallic haploid *S. cerevisiae* to cope with an unfavorable environment and to improve their survival rate for generations.<sup>18–20</sup> Pheromones, a type of sex hormone secreted by *S. cerevisiae*, serve as the yeast's mating signal, informing its partner to prepare for the beginning of cell fusion.<sup>18–24</sup> What will happen to the yeast cell if its partner does not arrive and this normal stimulation continues? From microscopic gene network (Figure 1), external signals are transmitted to Fus3 through a series of internal proteins such as prototype heterotrimeric GTP binding protein and the MAPK kinase cascade.<sup>25,26</sup> Then, Fus3 shuttles back and forth across the nuclear membrane, directly or indirectly activating genes for cell-cycle arrest (Far1) and polar growth (Bni1).<sup>27–35</sup> Thus, the current understanding of the pheromone-induced fate of yeast cells can be qualitatively summarized as the occurrence of cell-cycle arrest and polarized cell growth.<sup>36–38</sup>

In the context of exploring cell fate, previous studies have highlighted the significant role of cellular decision-making in determining the ultimate outcome of cells when exposed to various external stimuli.<sup>39–48</sup> It is important to note that while some of these studies primarily focused on quantifying binary outcomes, our study takes a comprehensive approach by quantifying multiple aspects of cell behavior over time. From a biological perspective, cell fate decisions can be conceptually characterized as the cascading transmission of signals along a static causal pathway.<sup>49–53</sup> However, the quantitative dynamics of cell fate decision-making over time during global responses at both the mesoscopic and microscopic levels remain poorly understood. Recent advances in live cell fluorescence imaging platforms have led to increasing focus on studying the dynamics of biological processes and the underlying molecular mechanisms in living cells.<sup>48,54–66</sup> Nevertheless, disruptions in the external environment can perturb the delicate balance of cellular activities and exacerbate internal imbalances in yeast cells, as living cells are complex non-equilibrium microsystems.<sup>67–75</sup> Therefore, quantifying these underlying cell fate decisions in response to external stimuli remains a significant challenge.

<sup>1</sup>College of Chemistry, Jilin University, Changchun, Jilin 130012, China<sup>2</sup>State Key Laboratory of Electroanalytical Chemistry, Changchun Institute of Applied Chemistry, Chinese Academy of Sciences, Changchun, Jilin 130022, China<sup>3</sup>Department of Chemistry and of Physics and Astronomy, State University of New York at Stony Brook, Stony Brook, NY 11794-3400, USA<sup>4</sup>Lead contact

\*Correspondence: liuqiong@ciac.ac.cn (Q.L.), jin.wang.1@stonybrook.edu (J.W.)

<https://doi.org/10.1016/j.isci.2023.107885>

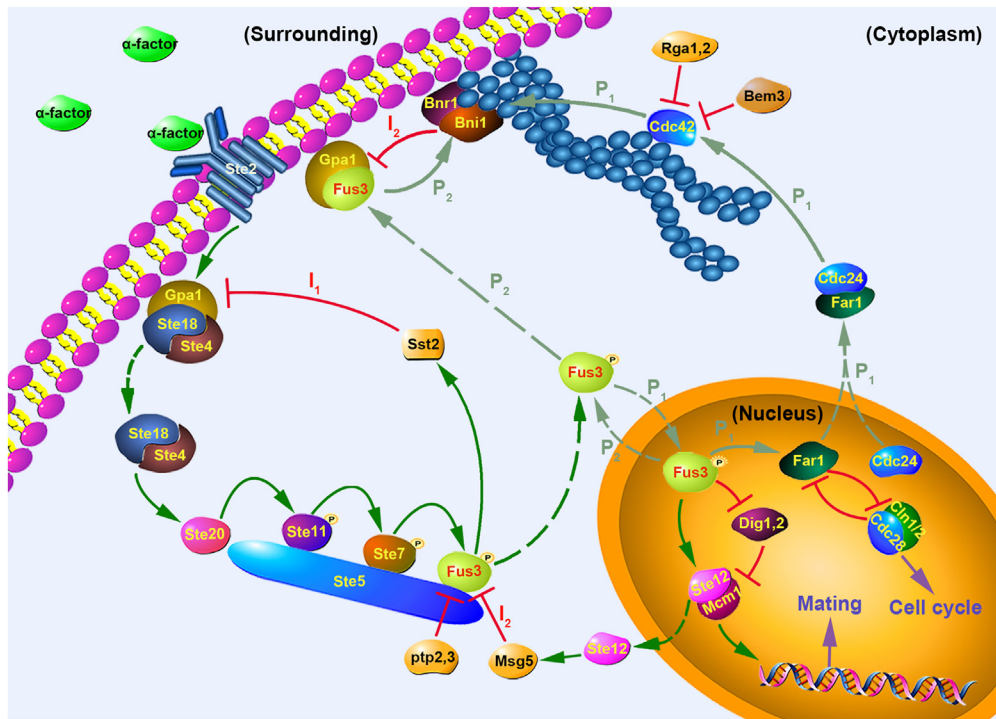


**Figure 1. Schematic diagram of the mating signal pathway of the yeast cell pheromone pathway**

The red horizontal line represents the inhibition of negative feedback; the green arrow represents the activation of positive feedback; the dashed arrow represents a shift in localization;  $I_1$  and  $I_2$  represent different negative feedback adjustment pathways; and  $P_1$  and  $P_2$  represent the two polar growth signaling pathways that are connected by light green arrows. The outline of the pathway is as follows: The binding of  $\alpha$ -factor to its transmembrane receptor Ste2 leads to activation of the heterotrimeric G protein complex consisting of Gpa1 ( $G\alpha$ ), Ste4 ( $G\beta$ ), and Ste18 ( $G\gamma$ ). This causes dissociation of the G $\beta\gamma$  dimer (Ste4/Ste18) from G $\alpha$  (Gpa1). The released G $\beta\gamma$  then recruits the PAK kinase Ste20 to the membrane and activates it. Ste20 initiates the MAPK cascade by phosphorylating the MAPKKK Ste11. Activated Ste11 phosphorylates the MAPKK Ste7, which then phosphorylates the MAPK Fus3. The activated Fus3 has two downstream effects: First, Fus3 directly phosphorylates and activates the formin Bni1, which nucleates actin cables for polarization. Second, Fus3 enters the nucleus and phosphorylates Ste12, a transcription factor that induces mating-specific genes. Fus3 also phosphorylates Far1, which inhibits the G1-S transition by binding to Cdc28-Cln2 complex. The Fus3-Far1 complex exits the nucleus and binds to Cdc24, promoting the activation of the Rho-GTPase Cdc42. Activated Cdc42 in turn stimulates Bni1.

Indeed, from a microscopic perspective, the cellular decision-making of yeast in response to mating information is accomplished through multiple feedback loops, not only including the positive feedback regulation mediated by Fus3 but also through certain negative feedback regulation that can effectively reduce the transcriptional output of this pathway.<sup>76–81</sup> After pheromone stimulation, there are two pathways that can lead to polar growth of the cells (Figure 1). The first path ( $P_1$ ) is “Fus3  $\rightarrow$  Far1/Cdc24  $\rightarrow$  Cdc42  $\rightarrow$  Bni1”.<sup>37,82–84</sup> This is realized by Fus3 entering the nucleus to activate Far1, which can escape from the nucleus to activate Bni1 indirectly. The second path ( $P_2$ ) is direct activation by Fus3 of Bni1 in the cytoplasm, “Fus3  $\rightarrow$  Bni1”.<sup>28,85</sup> In the process of these two polar growth pathways acting alone or in concert, the pheromone-induced self-activation of Fus3 (“Fus3  $\rightarrow$  Fus3”) facilitates the rapid transmission of the signals.<sup>86–89</sup> Activation of the pheromone pathway also induces multiple negative feedback loops, such as  $I_1$  (Sst2 and Gpa1)<sup>79–81,90–92</sup> and  $I_2$  (Msg5 and Bni1)<sup>28,77–81,93–95</sup> in the pathway. Only at high-dose pheromone levels is the negative feedback of the downstream Msg5 upregulated<sup>77</sup> and only at high concentrations of Bni1 is the activity of Fus3 indirectly reversed by Bni1.<sup>9,28,85,96,97</sup>

Here, by observing the multi-dimensional response at the single-cell level, we discovered the non-equilibrium steady states, which demonstrate the cell fates quantitatively, in response to different concentrations of pheromone. These steady states or cellular destinies include two gene expression levels, four growth rates, and four morphological fates. We quantified these responsive fates of the yeast cells in real time from various dimensions, including expression levels of Fus3 inside and outside of the nucleus, cell morphology, cell growth rate, and the concentrations of pheromone stimulation. Multiple states, as well as switching kinetic rates and pathways among them, were revealed, giving rise to a quantitative landscape of the mating response. The applications of landscape and flux theory to this biological system enabled us to quantify the non-equilibrium dynamics of the yeast cell mating responses. Our results established a global and physical framework for understanding cell fate decision-making and mating dynamics. Importantly, the logical links between molecular interactions and signal transduction proposed by our landscape model were validated experimentally, further supporting the robustness of our hypothesized molecular mechanisms governing the formation of these states. These molecular mechanisms establish the links between molecular events to cellular characteristics across scales. They allow for the real-time synchronization of intracellular signaling with their physiological growth and

morphological functions, bridging microscopic mechanisms and mesoscopic functions. To further elucidate these microscopic mechanisms, we conducted biochemical reaction simulations to demonstrate the emergence of these states. These findings shed new light on the global signaling mechanisms that govern how yeast determines its cellular fate in response to pheromone.

## RESULTS

### Quantifying the cellular decision-making threshold

Studies have shown that yeast, for which mating decisions are an all-or-none switch-like response, can automatically filter out very low-dose pheromone signals and only respond near a critical concentration or higher.<sup>92,98,99</sup> This is due to the fact that very low doses of pheromone induce insufficient accumulation of intracellular signals, such as Fus3, which are incapable of initiating the mating-readiness project.<sup>100–102</sup> To determine a pheromone concentration capable of arresting the cell cycle, we measured the fluorescence intensity of FUS3-GFP by flow cytometry in yeast cells incubated for 24 h with varying pheromone concentrations (Figures 2A and S1). According to the fitted statistics, the expression of Fus3 at a pheromone dose of 0.01–0.4  $\mu\text{M}$  showed unimodal distribution of the fluorescence intensities, indicating a homogeneous population of cells with similar expression levels of Fus3. However, at a pheromone concentration of 0.6  $\mu\text{M}$ , a bimodal distribution representing the bistable states gradually began to appear.

In order to comprehend the correlation between gene expression levels of Fus3 and the threshold of cellular response, the fluorescence intensity trajectories of Fus3 expression in single cells were associated with the microscopy-based cellular response under various pheromone concentrations over time. A microfluidic device was used to culture yeast under constant temperature conditions in real time. Using wide-field fluorescence microscopy with total internal reflection capabilities, we captured the real-time survival status and fluorescent signals of the yeast cells (Videos S1, S2, S3, S4, S5, S6, and S7). Compared to 0.7  $\mu\text{M}$  pheromone, the expression of Fus3 in the yeast cells did not fluctuate significantly at 0.2  $\mu\text{M}$ , resulting in its inability to inhibit cell budding reproduction (Figure 2B). However, the expression of Fus3 at a pheromone concentration of 0.7  $\mu\text{M}$  exhibited four stages: the initial stage (0– $b_1$ ), the adaptive stage ( $b_1$ – $b_2$ ), the stable stage ( $b_2$ – $b_3$ ), and the recovery stage ( $b_3$ – $b_4$ ), corresponding to the biological behavior of yeast cells at different stages. Therefore, the unimodal distribution of 0.01–0.4  $\mu\text{M}$  pheromone occurred when only the initial cells (0– $b_1$ ) were present in the flow cytometer sample. This very low dose of pheromone was unable to arrest the cell cycle from the beginning in yeast. If the pheromone had arrested the cell cycle of yeast cells from the beginning, but not for more than 24 h, some yeast cells would have resumed budding at a later stage. As demonstrated by the bimodal distribution of 0.4–1.5  $\mu\text{M}$  pheromone, the sample contained yeast cells in two distinct states ( $b_2$ – $b_3$  and  $b_3$ – $b_4$ ).

To validate the presence of bistability at the critical pheromone concentration (0.6  $\mu\text{M}$ ), we analyzed the scatter data obtained from flow cytometry, specifically the forward scatter (FSC) and side scatter (SSC). By visualizing the 3D scatterplot of FSC and SSC data (Figures 2C and S2), we gained insights into the cell size and granularity characteristics. At pheromone concentrations ranging from 0.01 to 0.4  $\mu\text{M}$ , the scatterplot showed a consistent cell size pattern, supporting the presence of a single-cell state. However, at concentrations between 0.6 and 1.5  $\mu\text{M}$ , the scatterplot exhibited distinct clusters, indicating the coexistence of different cell states characterized by different cell sizes. This observation directly supports our previous findings and reinforces the notion that the bistable states are a result of the presence of deformed cells and newly budding cells.

The results measured by flow cytometry were only rough estimates of critical mating decision thresholds, whereas microscopy of individual cells cultured in microfluidics revealed more precise cellular decisions. During culturing with varying concentrations of pheromone, we found that the time required for yeast cells to arrest their cell cycle was directly proportional to the pheromone concentration (Figure 2D). To further quantify the relationship between pheromone concentration and the duration of cell-cycle arrest, we conducted additional analysis by studying the time distribution during which cells remained arrested after surpassing the threshold volume until they resumed budding (Figure S3). The data clearly demonstrate that as the pheromone concentration increases, the yeast cells exhibit a longer duration of cell-cycle arrest. This distribution plot provides direct evidence to support the notion that higher pheromone concentrations lead to prolonged cell-cycle arrest in yeast cells. Furthermore, we observed another phenomenon: the duration of G1 cell-cycle arrest induced by different concentrations of pheromone had a limit. Although the use of microfluidic devices ensured a constant concentration of stimuli in the yeast cell's external environment, the cells were still able to regulate their response to external signals through gene expression levels, protein activity, and other mechanisms. As a result, even after being stimulated for a certain period, the yeast cells were capable of resuming budding reproduction.

### Two cell fate decision states reflected in the expressions of Fus3

To explore the yeast cell fate decision-making during the stable stage ( $b_2$ – $b_3$  in Figure 2B), the fluorescence intensity trajectories of Fus3 inside and outside the nucleus were plotted over time (Figures S3A, S4, and S5). The trajectories demonstrated that after approximately 600 min of yeast cell cultivation, Fus3 entered a stable stage where its fluorescence fluctuated around a certain value. In non-equilibrium statistical physics, the fluorescence intensity curve in this stable stage can be interpreted as a non-equilibrium steady state, whereas the rising phase of the first 600 min can be interpreted as a non-equilibrium non-steady state or the relaxation process of the response. To visualize the cell fate of yeast at the level of gene expression, the three-dimensional statistical distribution of Fus3 (cytoplasmic and nuclear fluorescent signals) was plotted during the non-equilibrium steady-state phases (Figures 3B and S6–S8). Clearly, the landscape of Fus3 displayed two peaks, which correspond to the two cell fates that existed both inside and outside the nucleus.

To comprehend the logical relationship between the cell fate at expression levels of Fus3 and pheromone-influenced signaling in the transduction process, we explored the biological mechanism underlying the emergence of these two Fus3 fates. We proposed that the two fates of

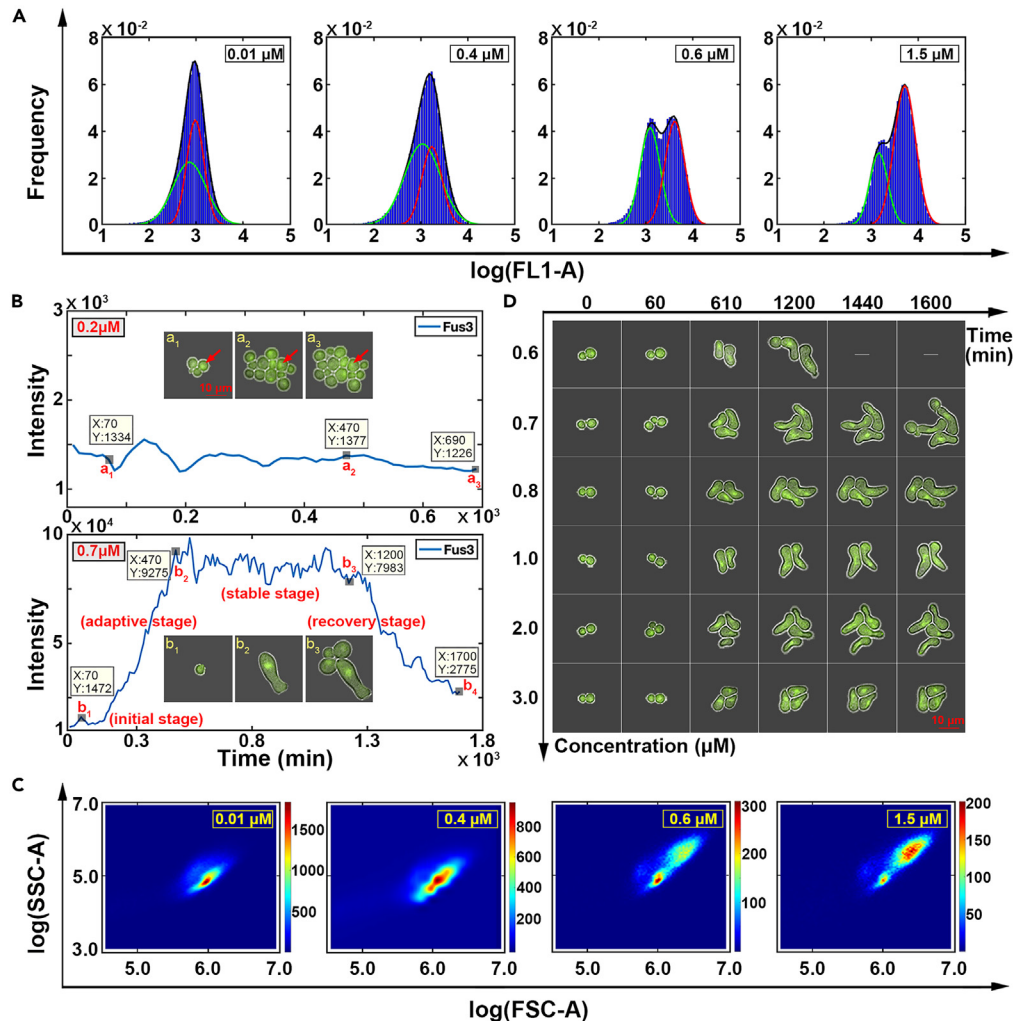


**Figure 2. A non-equilibrium biological model for cellular responses**

(A) The fluorescence intensity of *FUS3*-GFP was measured using flow cytometry. The yeast cells were cultured in YPD medium containing different concentrations of pheromone for 24 h. The x axis represents the logarithmic scale (base 10) of fluorescence intensity, specifically the FL1-A parameter in flow cytometry; FL1-A is a measurement channel in flow cytometry that captures the fluorescence emission of a specific fluorochrome or fluorescent protein; it reflects the intensity of *FUS3*-GFP fluorescence. The y axis represents the normalized probability density, indicating the relative frequency of intensity values within each histogram bin. Normalized method:  $\int P(x) dx = 1$ . The black curve represents the overall fluorescence intensity statistics, and the green and red curves represent the two fitted statistical peaks. The sample size for each pheromone concentration test was 105,000 yeast cells.

(B) *Fus3* gene expression was observed microscopically in response to 0.2  $\mu\text{M}$  and 0.7  $\mu\text{M}$  pheromone. The x axis represents the duration of exposure to the pheromone-containing medium. The y axis represents the fluorescence intensity of *FUS3*-GFP; and images  $a_1$ – $a_3$  and  $b_1$ – $b_3$  depict the living states of yeast cells as observed through a microscope at their corresponding times. For the 0.2  $\mu\text{M}$  fluorescence trajectory, the specific yeast cell it belongs to has been indicated with a red arrow.

(C) A 3D top view of the probability density distribution for dual-angle scattering data. The x axis represents the logarithmically transformed values of FSC-A, while the y axis represents the logarithmically transformed values of SSC-A. FSC-A (Forward Scatter-Angle) refers to the intensity of light scattered at a forward angle in flow cytometry; it reflects the size and complexity of cells or particles. SSC-A (Side Scatter-Angle) represents the intensity of light scattered at a side angle in flow cytometry; it provides information about the internal structure and complexity of cells. The z axis represents the probability density distribution, indicating the density of probability at each data point.

(D) The microscopically captured living state of yeast at various pheromone concentrations. The green fluorescence in cells represents the expression of *FUS3*-GFP; 60 min on the x axis represents the time when yeast cells were switched to a culture medium containing pheromone.

*Fus3* expression observed in signaling could be explained by a logical sequence involving functional depletion and feedback loops. First, functional depletion means that when the amount of *Fus3* in the nucleus was sufficient to arrest the cell cycle and activate the mating protein (“Outer. $P_1$   $\rightarrow$  Far1 & Ste12”), the excess *Fus3* was transported out of the nucleus for polar growth (“Outer. $P_1$   $\rightarrow$  Inner. $P_1$ ” and “Inner. $P_2$   $\rightarrow$  Outer. $P_2$ ”) (Figure 3C). Second, the feedback loop means that yeast actively regulated *Fus3* expression by activating or inhibiting signals.

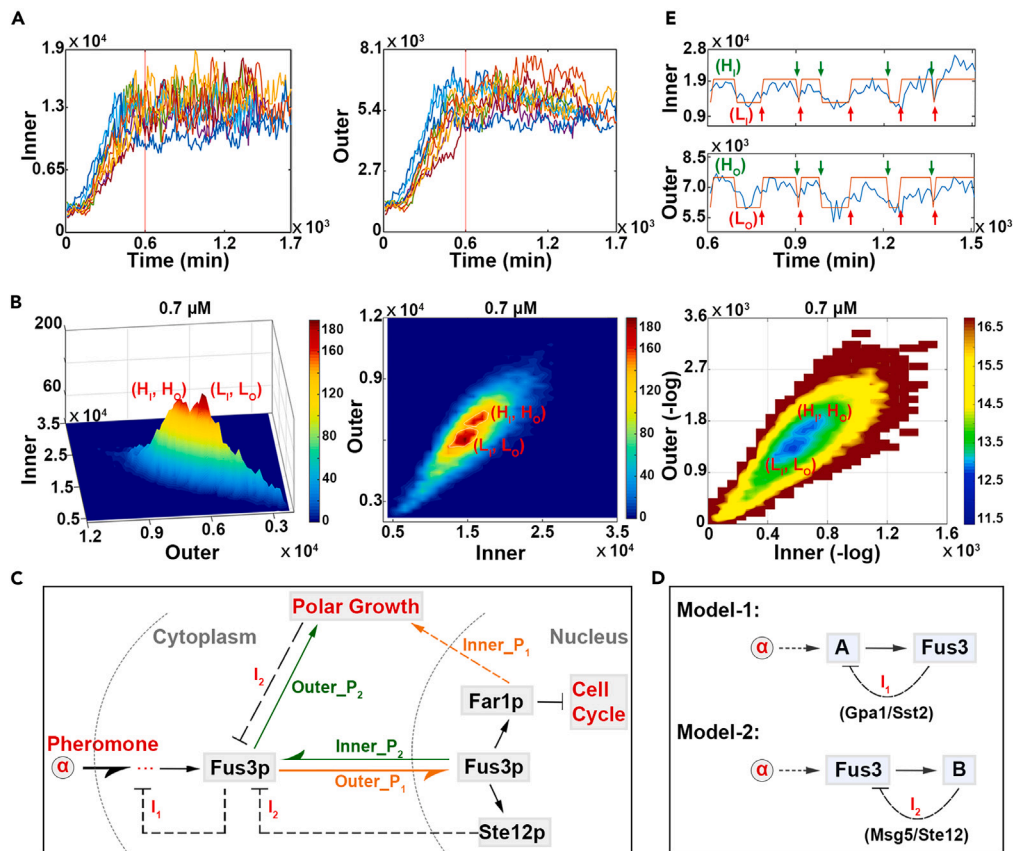


**Figure 3. The two steady states of expression levels of Fus3**

(A) Trajectories of fluorescence intensity of Fus3 at  $0.7 \mu\text{M}$  inside and outside the nucleus (only a portion shown). The red vertical line at 600 min was used to approximate the time node at which all cell fluorescence trajectories had entered a non-equilibrium steady state.

(B) Three-dimensional distribution graph of Fus3 fluorescence intensity inside and outside the nucleus of yeast cells in the stationary phase under different pheromone concentrations. On the left is the 3D distribution of fluorescence or the 3D population landscape, in the middle is the 2D histograms or the 2D underlying potential landscapes  $U$  ( $U = -\ln P$ ), which is also the population landscape; on the right is the 2D underlying potential landscapes  $U$  ( $U = -\ln P$ ). The sample sizes at steady state for each pheromone concentration are as follows:  $0.7 \mu\text{M}$  was equivalent to 21,335 cells,  $0.8 \mu\text{M}$  to 18,408 cells,  $1.0 \mu\text{M}$  to 23,041 cells,  $2.0 \mu\text{M}$  to 36,886 cells, and  $3.0 \mu\text{M}$  to 18,276 cells.

(C) Diagram illustrating the molecular mechanism by which yeast cells respond to pheromone. The Outer\_P<sub>1</sub> represents the indirect pathway taken by Fus3 from the cytoplasm to the nucleus in order to inhibit the cell cycle; Inner\_P<sub>1</sub> represents the indirect pathway by which Fus3 in the nucleus promoted polar growth; Outer\_P<sub>2</sub> represents the direct pathway of Fus3 in the cytoplasm for polar growth; Inner\_P<sub>2</sub> represents the direct pathway for the transfer of Fus3 from the nucleus to the cytoplasm for polar growth; I<sub>1</sub> and I<sub>2</sub> represent the inhibitory effects of the negative feedback regulation; and the two gray dashed lines represent the cell membrane and the nuclear membrane. “ $\alpha$ ” stands for  $\alpha$ -factor pheromone. The signaling cascade follows the following logic: Upon receiving sufficient external signals ( $\alpha$ -factor), yeast cells activate Fus3, leading to a significant increase in phosphorylated Fus3 levels. Subsequently, activated Fus3 translocates into the cell nucleus (Outer\_P<sub>1</sub>), initially engaging the branch involved in cell cycle inhibition, namely, Fus3  $\rightarrow$  Far1. Once the cell cycle is inhibited, activation of mating-specific proteins like Ste12 ensues. Within the nucleus, the activated Far1 not only contributes to cell-cycle arrest but also facilitates the activation of the first polarity growth pathway (Inner\_P<sub>1</sub>) upon exiting the nucleus. As the nuclear Fus3 reaches a threshold level, excess Fus3 exits the nucleus and triggers Bni1 activation to facilitate polarized growth (Inner\_P<sub>2</sub>). Concurrently, cytoplasmic Fus3 initiates the second polarity growth pathway (Outer\_P<sub>2</sub>).

(D) Schematic representation of two negative feedback models for regulating Fus3 gene expression. A and B represent, respectively, two different types of proteins that interact with Fus3 in the signaling pathway; “ $\alpha$ ” stands for  $\alpha$ -factor pheromone.

(E) Fluorescence intensity trajectories of Fus3 inside and outside the nucleus over time under non-equilibrium steady state. The red line represents the fitting by the hidden Markov model to distinguish high- and low-expression states. Arrows indicate spontaneous state switching events between the high state (H<sub>i</sub>/H<sub>o</sub>) and low state (L<sub>i</sub>/L<sub>o</sub>). The x axis is shared between the two panels to optimize figure clarity. The high and low states were distinguished by hidden Markov modeling of the fluorescence trajectories, with iterative optimization of model parameters to ensure global convergence. The expression fate at each time point was determined by the relative probability and transition dynamics between the two expression states.

**Table 1. Correlation coefficients of fluorescence trajectories**

Pheromone doses ( $\mu\text{M}$ )	0.7	0.8	1.0	2.0	3.0
Correlation (inside & outside)	0.8321	0.8647	0.8446	0.7752	0.8879

The "Pearson correlation coefficient" between the intranuclear and extranuclear fluorescence intensity trajectories at various pheromone concentrations.

Previously, experimentally validated feedback loops were categorized into two models: " $A \rightarrow \text{Fus3} \rightarrow A$ " focuses primarily on the pathways involving Gpa1 and Sst2, whereas " $\text{Fus3} \rightarrow B \rightarrow \text{Fus3}$ " focuses primarily on the pathways involving Ste12 and Msg5 (Figures 1 and 3D).

This dynamic sequential mechanism results in two behaviors: the highly coordinated expression levels of Fus3 inside and outside the nucleus, and the alternation of the two fates. As experimental evidence for our proposed molecular mechanism, we observed the existence of two behaviors. We revealed a correlation between intra- and extra-nuclear fluorescence intensities using Pearson's coefficient. A linear correlation of approximately 0.80 between these two types of fluorescence trajectories at various pheromone concentrations indicated a strong synergy between them (Table 1). In addition, using a hidden Markov chain model, we characterized the two cellular fates using gene expression levels by fitting the fluorescence trajectories into high states ( $H_I, H_O$ ) and low states ( $L_I, L_O$ ) (Figure 3E). The fitted red line in Figure 3E demonstrates that the two trajectory fates (high and low states) inside and outside the nucleus could switch to each other, supporting our logical interpretation of the state switching above.

### Uncovering the physical characteristics of cellular decision-making landscapes

To uncover the physical characteristics of the underlying bistable landscapes, we employed a hidden Markov chain model to compute the transition probability, transition rate, and residence time between the two gene expression fates. In the non-equilibrium steady state, the steady-state probability can be used to quantify the population landscape  $P$  or the potential landscape  $U^{68,103-105}$ , where  $U$  is defined as the negative logarithm of the steady-state distribution  $P$  of gene expression,  $U = -\ln P$ . As can be seen, the population and potential landscapes ( $P$  and  $U$ ) at various pheromone concentrations have two basins of attractions that are separated by barriers (Figures 3B and S6–S8). The transition probabilities and residence times of the two expressions of FUS3, high state ( $H_I, H_O$ ) and low state ( $L_I, L_O$ ), can be determined through the statistical analysis of the experimental data fitted by the hidden Markov chain model. The transition rate can be derived from the transition probability, whereas the barrier height is determined by fitting two peaks into the landscape. The barrier height is determined by the depth of the basin on the potential energy landscape ( $U = -\ln P$ ) obtained directly from the statistical histogram ( $P$ ) of the fluorescence signals of the gene expressions (Table 2).

At pheromone concentrations between 0.7 and 0.8  $\mu\text{M}$ , the barrier heights of the low state ( $L_I, L_O$ ) were less than those of high state ( $H_I, H_O$ ), whereas the opposite was true between 1.0 and 3.0  $\mu\text{M}$  (Figure 4A). In physics, the transition between steady states becomes harder as the barrier height increases, resulting in a longer residence time.<sup>103,104</sup> Based on the statistical analysis of experimental data, it was observed that the distribution of barrier heights between high and low states at different pheromone concentrations was consistent with the distribution of their corresponding residence times (Figures 4A and 4B). The correlation coefficient between barrier heights and residence times for all concentrations was 0.8806, indicating that they were significantly positively correlated (Figure 4C). This substantiates the statistical non-equilibrium physics claims regarding barriers and residence time. From a statistical physics perspective, the quantified barrier heights directly correlate with the relative stability and kinetic transition rates between the two expression states, providing a physically grounded characterization of the multi-stability.

To explore the biological implications of the landscape physical characteristics, we calculated the distribution of their ratios for two gene expression fates as a function of pheromone concentration. The opposite trend of the transfer rate ratio ( $k_{H_I}/k_{L_I}$ ) relative to the barrier height ratio or the residence time ratio (high/low, H/L) in response to changes in pheromone concentration indicated that transition rates were lower the deeper the attraction basin (Figure 4D). To better comprehend this relationship, the potential landscape topographies under varying pheromone concentrations were illustrated (Figure 4E). Compared to a pheromone concentration of 0.7  $\mu\text{M}$ , 0.8  $\mu\text{M}$  had a deeper attraction basin for its high state than for its low state, making the transition from low to high states easier than that from high to low states. The yeast's cellular decision-making at the level of gene expression was consequently more likely to remain in the high state than in the low state. At 1.0–3.0  $\mu\text{M}$ , the attraction basin of the low state was deeper than that of the high state, leading to the yeast's preference to remain in the low state. In general, as pheromone doses increase from low to high, the basin of the high-potential state gradually becomes shallower, whereas the basin of the low potential state gradually becomes deeper. The increased height of the low-state potential barrier is due to the negative feedback regulation that is able to inhibit the expression of Fus3, resulting in a greater number of yeast cells in a low-expression state. This supports the biological notion that high-dose pheromone elicits a stronger negative feedback response compared to the low-dose pheromone. In summary, the opposite trend of barrier heights and residence times of the high and low states validated that the experimentally observed multi-stability originates from the inherent interactions of the signaling network, giving rise to the emergence of the underlying non-equilibrium landscape, which encodes the robustness and inter-transition dynamics of each expression state.

### Quantifying the cellular deformation rate in polar growth

During the time-dependent deformation of the cell, we observed that not only did the top, representing the region along the cell's elongation axis or polarized growth direction, exhibit growth, but other parts of the cell also underwent slight widening as the yeast stretched forward

**Table 2. Physical characterization of gene expression landscapes**

Pheromone doses ( $\mu\text{M}$ )		0.7	0.8	1.0	2.0	3.0
Transition probability $P = \begin{pmatrix} P_{LL} & P_{LH} \\ P_{HL} & P_{HH} \end{pmatrix}$	$P_{LL}$	0.69	0.74	0.5369	0.5502	0.6143
	$P_{LH}$	0.31	0.26	0.4631	0.4498	0.3857
	$P_{HL}$	0.3711	0.4251	0.5053	0.445	0.3686
	$P_{HH}$	0.6289	0.6289	0.6289	0.6289	0.628
	Transition rate	$k_{LH}$	0.0623	0.0717	0.1803	0.112
	$k_{HL}$	0.052	0.0439	0.1652	0.1132	0.0718
Residence time (min)	Low ( $L_i, L_o$ )	357.43	270	691.5	947.98	750.74
	High ( $H_i, H_o$ )	498.17	941.84	539.63	301.44	212.3
Barrier height	Low ( $L_i, L_o$ )	0.1131	0.0997	0.1323	0.2175	0.1716
	High ( $H_i, H_o$ )	0.1371	0.1657	0.1125	0.0285	0.0451

The transition probability, transition rate, residence time, and barrier height between the high and low states at various pheromone concentrations.

(Videos S1, S2, S3, S4, S5, S6, and S7). To accurately measure the spatiotemporal change rate of the cell morphology, we used a circular filling pattern to segment the yeast cells (Figure 5A). To quantify the various cell deformations that occur during cell growth, we considered a value ( $H_n$ ) comparable to the harmonic mean to characterize the cell morphology.  $H_n$  equals the sum of the reciprocal radii of the filled circles multiplied by the number of filled circles, i.e.,  $H_n = n\left(\frac{1}{R_1} + \frac{1}{R_2} + \dots + \frac{1}{R_n}\right)$ . The significant advantage of this parameter is that it is particularly sensitive to small morphological changes at various locations of the cell, allowing differential non-directional normal growth and directional polar growth (i.e., lateral growth and longitudinal growth) to be characterized in real time.

From the real-time trajectory of the changes in the cell morphology, as measured by the  $H_n$  of the cell-filled circles, we found that there were roughly four types of cell shape changes. According to the definition of  $H_n$  describing the cell morphology, the rising phase ( $t_1 - t_2$ ) of the curve primarily represents the change in cell length, whereas the falling phase ( $t_3 - t_4$ ) primarily represents the change in cell width. At the ( $t_2 - t_3$ ) and ( $t_4 - t_5$ ) phases, the slopes of the two curves are close to zero, indicating that cell morphology changes were minimal or non-existent (Figure 5B). We collected the statistics on the distribution of the cell growth rates or deformation rates (Figures 5C and S9). When the positive and negative values were differentiated, it was evident that the cell growth rate could be divided into four states: the lateral-fast rate, the longitudinal-fast rate, the lateral-slow rate, and the longitudinal-slow rate. Among them, L and W represented the presence and absence of direction in cell deformation, or the length and width, respectively. F and S represent the magnitude of the “driving force” in cell deformation, or the fast and slow growth rates, respectively.

To explore the molecular mechanisms underlying these four growth rates, we took both the direction (L and W) and force (F and S) of cell growth into account. Many studies have shown that Fus3 and Far1, which determine the direction of cell growth along its long axis, are essential genes for bud formation during polar cell growth, and their absence results in mis-localization of shmoo projections.<sup>82,83,85,106</sup> Thus, the indirect pathway ( $P_1$ : “Fus3  $\rightarrow$  Far1/Cdc24  $\rightarrow$  Cdc42  $\rightarrow$  Bni1”), which is more directional than the direct pathway ( $P_2$ : “Fus3  $\rightarrow$  Bni1”), is the leader signaling pathway for longitudinal cell growth. Given that the  $P_1$  pathway requires the sequential activation of multiple proteins and that proteins such as Fus3, Far1, and Cdc24 must be transported into or out of the nucleus, we proposed that the  $P_2$  pathway had a quicker response speed to stimulate cell growth than did the  $P_1$  pathway (Figure 5D). Consequently, the temporal delay in the actions of these two pathways resulted in  $P_2$ -dominated undirected growth (model W:  $P_2$ ), followed by the two growth pathways co-stimulating the cell’s polar growth (model L:  $P_1 + P_2$ ) once the  $P_1$  pathway was fully functional. In addition, we proposed that F and S corresponded to the high and low states in Fus3, respectively. When Fus3 was at a high state ( $H_i, H_o$ ), there was enough Fus3 to stimulate growth (model F). Following entry into the low state ( $L_i, L_o$ ), only a relatively small amount of Fus3 was available for polar growth (model S).

To confirm that there was indeed a time lag in multi-level protein signaling, we constructed a dual-fluorescence system (CDC24-GFP\_FUS3-RFP strain), in which CDC24 was linked to the green fluorescent protein (S65T) and FUS3 was linked to the red fluorescent protein (yomCherry) (Figure 5E, Videos S8, and S9). Taking into account the order of signal transduction in yeast in response to pheromone, the expression levels of Fus3 and Cdc24 would achieve the highest degree of correlation or match after a certain time lag. We employed cross-correlation analysis to compare the lag times of various activation sequences between different combinations of fluorescence trajectories: intranuclear Fus3 and intranuclear Cdc24, intranuclear Fus3 and extranuclear Cdc24, extranuclear Fus3 and intranuclear Cdc24, and extranuclear Fus3 and extranuclear Cdc24 (Figure 5F). The concept of cross-correlation allows us to examine how the sequence of fluctuations in Fus3 intensity aligns with Cdc24 intensity over time, indicating potential lag times or delays in their activation sequences. The figure shows that the lag time between Fus3 in the nucleus and Cdc24 (red curve) reaching a maximum correlation was approximately 120 min, while the lag time between Fus3 outside the nucleus and Cdc24 (blue curve) reaching a maximum correlation was approximately 300 min. The fact that the lag time of Fus3\_in and Cdc24\_in/out (red curve) in the figure was shorter than that of Fus3\_out and Cdc24\_in/out (blue curve) confirms the existence of a temporal delay effect in multi-level signaling and provides direct evidence for the temporal distinction in the functioning of the two growth pathways.

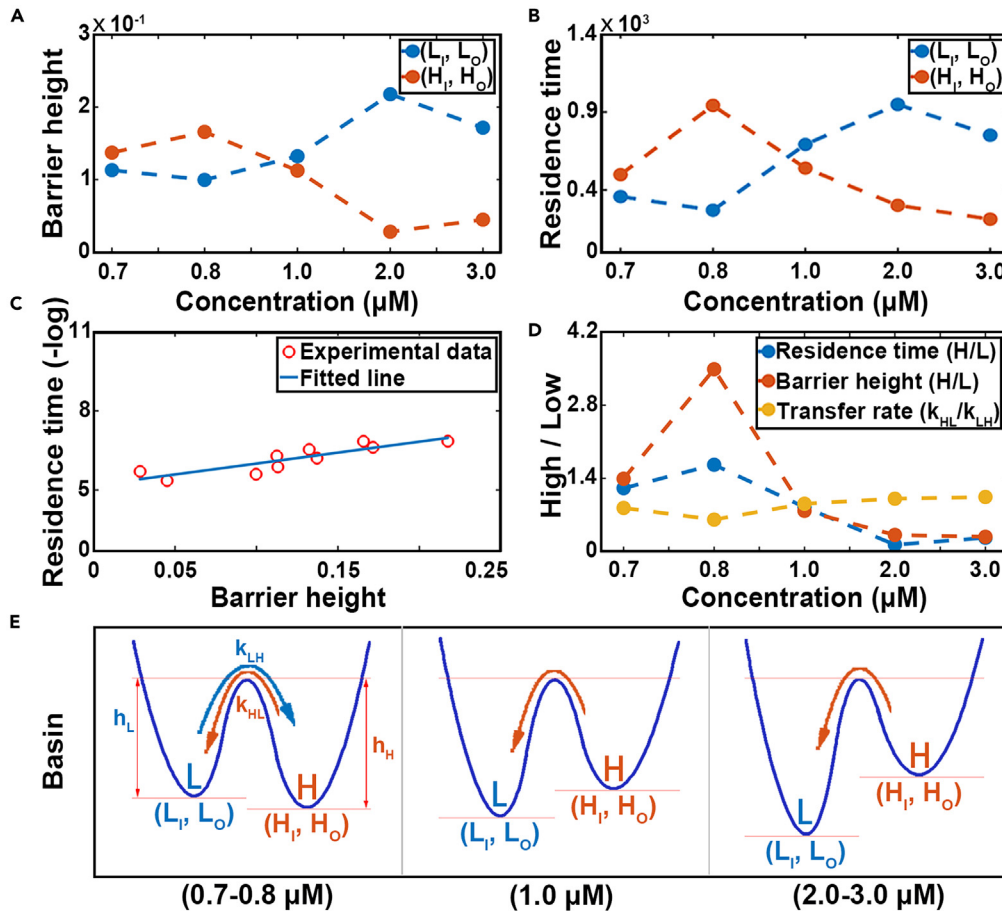


**Figure 4. The physical characteristics of cellular decision-making landscapes**

(A) Trends in the statistical distribution of barrier heights for high and low states at varying pheromone concentrations.

(B) Trends in the statistical distribution of residence time for high and low states at varying pheromone concentrations. The residence time represents the average duration the system stays in a particular state among all trajectories simulated using Markov chain modeling. The residence time is measured in minutes.

(C) Correlation analysis between residence time and barrier height. The red circles are the data points; the blue line is the fitted line of the data.

(D) The ratio of the physical characteristics of high and low states at various concentrations. The  $k_{LH}$  is the transition rate from a low state to a high state;  $k_{HL}$  is the transition rate from a high state to a low state.

(E) Simple schematic diagram of the potential landscape topography under different pheromone dosages. L stands for the low state, H stands for the high state;  $k_{LH}$  and  $k_{HL}$  are the transition rates between the low state and the high state, respectively;  $h_L$  and  $h_H$  represent the respective barrier heights of the low and high states, respectively.

By taking the growth rate absolute value, we divided the four states into fast growth rate and slow growth rate categories (Figures 5G and S10). To confirm that the two forces (F and S) corresponded to the high and low states of Fus3, respectively, the cell growth rate states and Fus3 gene expression states were measured as the cell polar growth changed over time. According to the proportion of statistics in the figure, the high (expression) state was primarily contained within the fast (growth) state, whereas the low (expression) state was primarily contained within the slow (growth) state (Figure 5H and Table 3). Consequently, this also provided quantitative experimental evidence for the cellular growth rate molecular mechanism.

### Quantifying the four morphological fates and the phase transition trend

The morphological trajectory of the cell shape over time as described by  $H_n$  fluctuated continuously within a given range (Figure 5B). Using a hidden Markov chain model to fit the time-varying trajectories of cell morphology, yeast cells at different pheromone concentrations exhibited four distinct morphological fates. These four morphological fates corresponded statistically to the four peaks in the distribution of all cell shapes ( $F_1$ – $F_4$ ) (Figures 6A and S11). Due to the fact that  $H_n$  is a parameter that is extremely sensitive to changes in the size and number of filled circles within the cell, minute variations in the length or width of a portion of the cell observed through a microscope can result in the cell being classified as having a different morphological fate (Figure 6B). We proposed, on the basis that cell morphology is an accumulation in

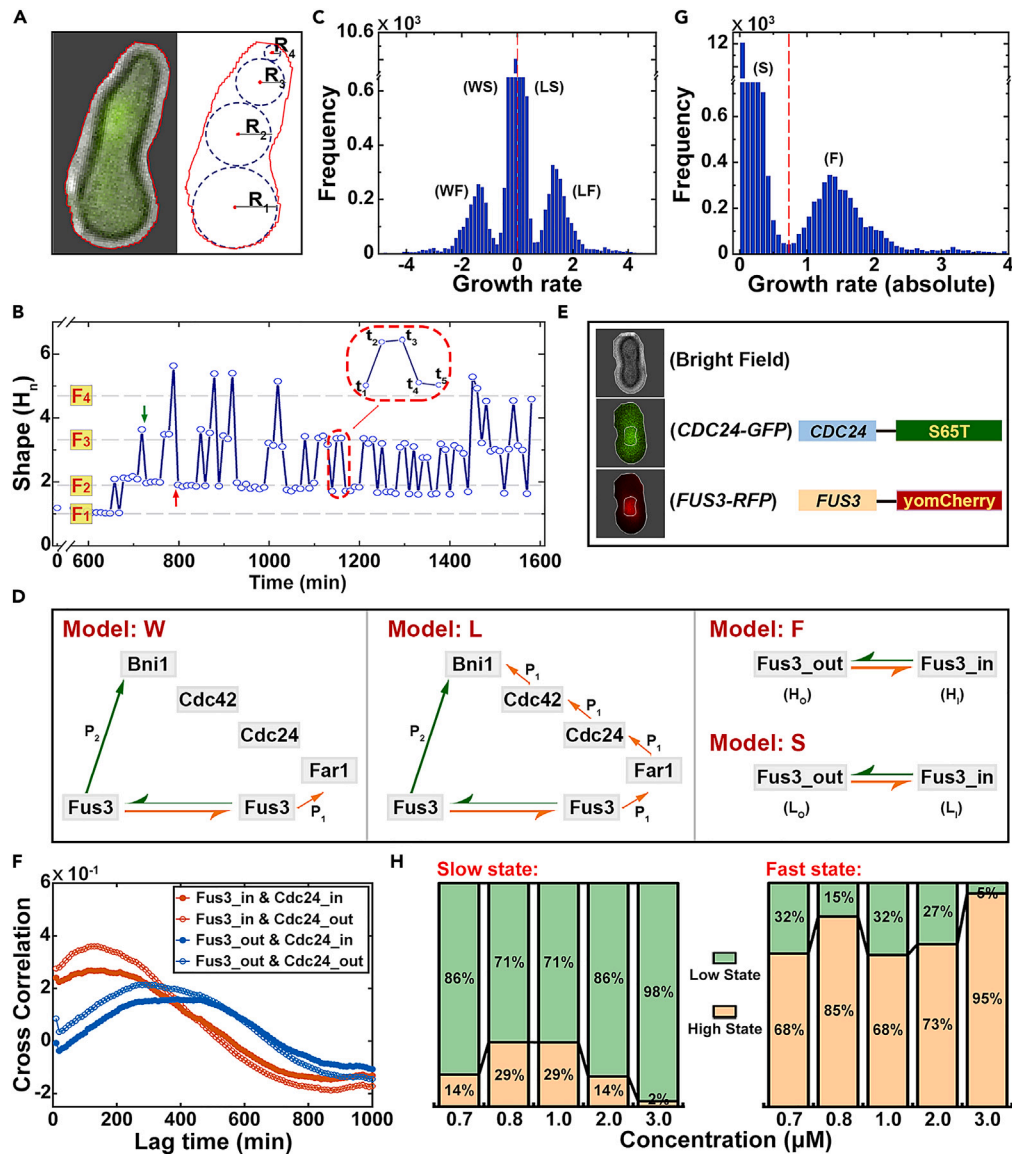


**Figure 5. Quantification of the deformation of yeast cells during polar growth**

(A) A simple diagram of cell shapes with circle filling patterns. The image on the left depicts a yeast cell cultured for 1,020 min in a medium containing 0.7  $\mu\text{M}$  pheromone; the red line indicates the contour of the cell; the image on the right is the filling model for the image on the left;  $R_1 - R_4$  are the radii of the circle.

(B) Real-time trajectory of the cell morphology ( $H_n$ ) at 0.7  $\mu\text{M}$  under non-equilibrium steady state.  $F_1 - F_4$  indicate the four distinct cell morphological fates. The horizontal dashed lines mark the approximate centers of the fates. Arrows highlight spontaneous state switching events between fates  $F_3$  to  $F_2$  (green) and  $F_2$  to  $F_4$  (red). The inset shows a magnified view of the trajectory over time points  $t_1 - t_5$ . Cell morphologies during the initial non-equilibrium non-steady-state period before 600 min are omitted.

(C) The distribution statistics of the cell growth rate at 0.7  $\mu\text{M}$ . The red dashed line serves as the dividing line between positive and negative data. WF and LS represent the lateral-fast and lateral-slow rates, respectively; LF and WS represent the longitudinal-fast and longitudinal-slow rates, respectively.

(D) Schematic illustration of the molecular mechanism underlying the formation of the four growth rates. Model W indicates that the polar growth pathway  $P_1$  is not yet connected, so only the  $P_2$  pathway operates; Model L depicts the cooperative operation of polar growth pathways  $P_1$  and  $P_2$ . Models F and S describe the polar growth patterns of the two growth forces, which correspond to the high and low states of Fus3, respectively.

(E) Dual fluorescent protein system in yeast. The three images on the left, from top to bottom, depict bright field cells, cells excited at 488 nm, and cells excited at 561 nm. The white circle within the cell represents the nucleus boundary; S65T and yomCherry are the fluorescent proteins that were linked to *CDC24* and *FUS3*, respectively.

**Figure 5. Continued**

(F) Cross-correlation of two levels of gene expression at distinct positions. Gene\_in and gene\_out represent the gene expression levels inside and outside the nucleus, respectively. The red curve represents the cross-correlation between Fus3\_in and Cdc24\_in/out, while the blue curve corresponds to the cross-correlation between Fus3\_out and Cdc24\_in/out.

(G) Statistical graph of the distribution statistics of the absolute value of the cell growth rate at 0.7  $\mu\text{M}$ .

(H) The proportion of high-state and low-state data present in high and low states at various pheromone concentrations.

growth, that the molecular mechanisms underlying the formation of the four morphological fates were dependent on the different capacities of cells to grow laterally and longitudinally. To test the claim that four morphological fates were formed, the synergistic effect of growth ability in both directions was calculated. The lateral growth capacity of cells was expressed by the rate of change of the average radius of the filled circle within the cell, whereas the longitudinal growth capacity was expressed by the rate of change of the sum of the radii of the filled circle. The existence of four distinct states in the cooperative distribution of the two data, as depicted in the figure, strongly suggested that the capacity to grow in different directions is a crucial factor in determining cell morphology (Figures 6C and S12).

Notably, a phase transition trend from four states to a dominant state in the cell morphology distribution between 0.7 and 3.0  $\mu\text{M}$  was revealed (Figure 6A). Moreover, the morphology of the cells observed under a microscope at a concentration of 3.0  $\mu\text{M}$  was significantly smaller than that observed at other concentrations (Figure 6B). By measuring the average cell length, it is possible to conclude that a high-dose pheromone concentration (3.0  $\mu\text{M}$ ) disrupted the monotonic linear trend observed at low doses (0.7–2.0  $\mu\text{M}$ ) (Figures 6D and Table 4). The microscopic explanation of this phase transition trend is the enhancement of negative feedback regulation under high doses ( $I_2$ ), suppressing the second polar growth pathway ( $P_2$ ) (Figures 1 and 3C). Under high pheromone concentration (3.0  $\mu\text{M}$ ), there was a significant accumulation in state  $F_2$ , while the morphologies of the other three cell fates ( $F_1$ ,  $F_3$ , and  $F_4$ ) decreased abruptly. This change is likely attributed to impaired  $P_2$  function (Figures 6A and S11).

To explain the underlying physical mechanism of the observed phase transition trend, where the four morphological fates undergo a transition toward a dominant fate in state  $F_2$ , we employed net flux analysis to quantify the degree of nonequilibrium in the cellular morphological system (Tables 5, 6, 7, 8, and 9). From the cell morphological trajectories analyzed by the hidden Markov chain model, we determined the transition probability between various cell morphologies. The sum of the three net fluxes, which was obtained by decomposing the probability loops in the transition matrix, was used to represent the degree of the detailed balance collapsed in the cellular morphological system (Figure 6E). As the concentration of pheromone increased, the intensity of the net flux decreased first and then increased, exhibiting a significant phase transition trend at 3.0  $\mu\text{M}$ . Since the net flux is rotational due to its steady-state nature under local probability conservation, it tends to destabilize the point attractors. Therefore, the significant changes in net flux can lead to the instability of the cell attractor states, giving rise to possible phase transition trend. The quantification of this non-equilibrium dynamic explains the physical mechanism by which the phase transition trend in a morphological system was caused by the enhanced capability of the yeast cells negative feedback regulation at high doses.

**Simulations for the signal transduction and the cell growth**

Based on the functional and quantitative regulation obtained from databases, such as KEGG (Kyoto Encyclopedia of Genes and Genomes, <https://www.kegg.jp/>), SGD (the Saccharomyces Genome Database, <https://www.yeastgenome.org/>), and EVEX (<http://evexdb.org/>), we developed a simplified model of signal transduction in the context of global gene regulatory networks. This model simulated a series of biochemical reactions with the Gillespie algorithm<sup>107–109</sup> (Tables S1–S3). By simulating the biochemical reactions associated with the pheromone pathway in yeast cells, the expression levels of Fus3 and the distribution of cell morphology were determined. Fus3 gene expression obtained from biochemical reaction results displayed a two-state distribution inside and outside of the nucleus, validating our understanding of the molecular mechanism underlying the bimodal fluorescence state within the context of the global response (Figure 6G). Meanwhile, the Bni1 produced by the reactions simulated the dynamic process of cell growth. Although both the growth pathways ( $P_1$  and  $P_2$ ) were involved in the process of cellular length and width growth, the relative weights of the pathways that grow in the two directions were significantly

**Table 3. The proportional distribution of high state ( $H_1, H_0$ ) and low state ( $L_1, L_0$ ) in two growth rates**

Pheromone doses ( $\mu\text{M}$ )	$\frac{FH}{(FH+FL)}$	$\frac{FL}{(FH+FL)}$	$(FH + FL)$	$\frac{SH}{(SH+SL)}$	$\frac{SL}{(SH+SL)}$	$(SH + SL)$
0.7	0.6847	0.3153	13888	0.1433	0.8567	7447
0.8	0.8500	0.1500	5027	0.2879	0.7121	13381
1.0	0.6782	0.3218	1157	0.2872	0.7128	21884
2.0	0.7266	0.2734	2249	0.1353	0.8647	34637
3.0	0.9530	0.0470	1679	0.0244	0.9756	16597

“FH” denotes the “High state” in the “Fast growth rate”; “FL” denotes the “Low state” in the “Fast growth rate”; “SH” denotes the “High state” in the “Slow growth rate”; “SL” denotes the “Low state” in the “Slow growth rate”; “FH + FL” and “SH + SL” represent fast and slow growth rate data volumes.

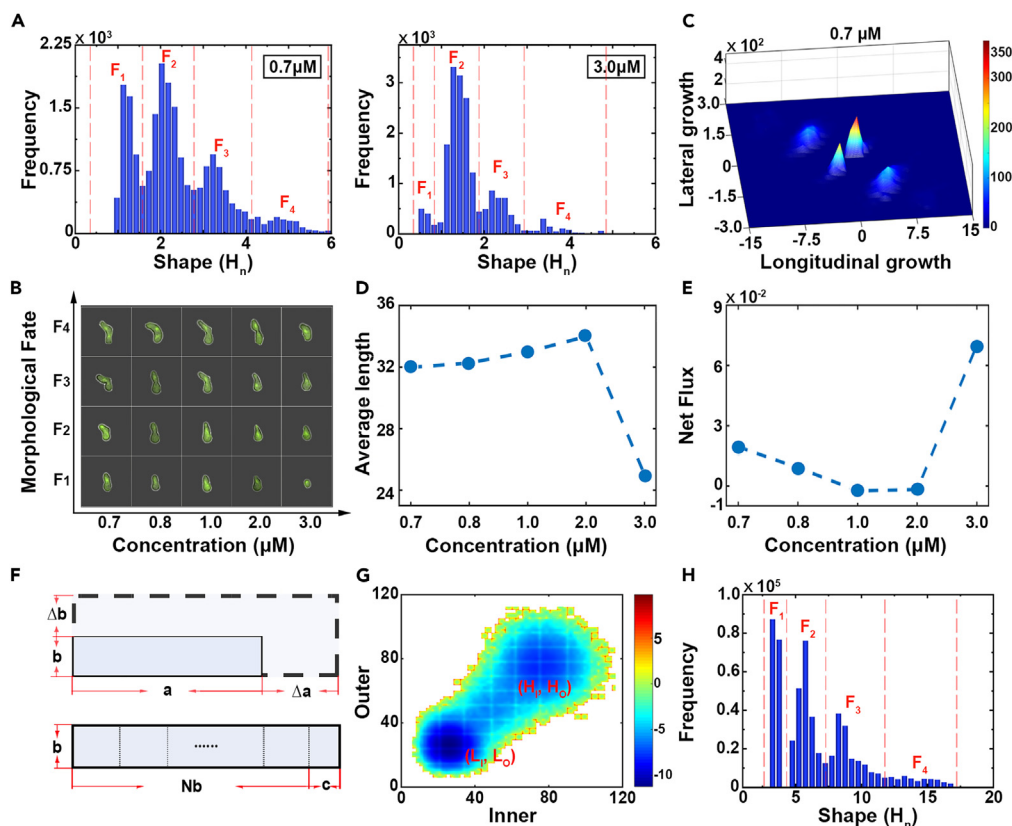


**Figure 6. The interpretation of the different cell morphological fates**

(A) Statistical distribution of the cell morphology at 0.7 and 3.0  $\mu\text{M}$ . The red dashed lines roughly correspond to the boundary between distinct cell morphological fates;  $F_1$ – $F_4$  represent the four cell morphological fates.  
 (B) Photographs taken with a fluorescence microscope of cells exhibiting four distinct morphological fates in response to varying pheromone concentrations.  
 (C) The synergistic effect of both lateral and longitudinal cell growth capabilities at a pheromone concentration of 0.7  $\mu\text{M}$ . The x axis represents the ability of the cells to grow longitudinally, as indicated by the rate of change in the sum of the radii of the filled circles within the cells, i.e.,  $(R_1+R_2+\dots+R_n)'$ ; the y axis represents the ability of cells to grow laterally, as indicated by the rate of change in the average radius of the filled circles within the cells, i.e.,  $(\frac{R_1+R_2+\dots+R_n}{n})'$ .  
 (D) Changes in the average cell length as a function of pheromone concentration.  
 (E) The sum of the net fluxes among the four cell morphologies at various pheromone concentrations.  
 (F) The scheme for the simulated cell growth; a represents the length of the cell;  $\Delta a$  is the increased length of the cell; b represents the width of the cell; and  $\Delta b$  is the increased width of the cell; the scheme of the  $H_n$  calculation; c is the remainder of the cell length divided by b; N represents the number of b.  
 (G) Distribution graph of the negative log of the value of the Fus3 fluorescence intensity inside and outside the nucleus of yeast cells in the stationary phase using simulation.  
 (H) The distribution of the cell morphology ( $H_n$ ) using simulation.

different. Therefore, we simply defined Bni1\_in produced by the  $P_1$  pathway that plays a major role as the longitudinal growth and Bni1\_out produced by the  $P_2$  pathway as the lateral growth.

In this simulation, a denotes the longitudinal length of the yeast cell, while b denotes the lateral length of the yeast cell (Figure 6F). Each iteration increased the longitudinal and lateral lengths of the yeast cells by  $\Delta a$  and  $\Delta b$ , respectively.  $\Delta a$  is proportional to “PBni1\_in” and inversely proportional to b;  $\Delta b$  is proportional to “PBni1\_out” and inversely proportional to a, that is,  $\Delta a = \frac{r_a(\text{PBni1\_in})}{b}$ ,  $\Delta b = \frac{r_b(\text{PBni1\_out})}{a}$ . The value N corresponds to the rounding operation of  $\frac{a}{b}$ , i.e.,  $[\frac{a}{b}]$ , and c represents the amount remaining after rounding. The  $H_n$  is  $(N + 1)(N/b + 1/c)$ . As predicted by the simulation of the cell growth process, the distribution of cell morphology revealed four distinct fates, which corresponded to the experimental observations (Figure 6H).

**Table 4. The average length of yeast cells at different pheromone doses**

Pheromone doses ( $\mu\text{M}$ )	0.7	0.8	1.0	2.0	3.0
Average length	31.98	32.27	32.99	33.99	25.01

**Table 5. The quantitative parameters in the net flux theory**

Pheromone dose ( $\mu\text{M}$ )	0.7
Number of transitions	$N_{(0.7\mu\text{M})} = \begin{pmatrix} 13536 & 373 & 0 & 254 \\ 229 & 0 & 0 & 140 \\ 232 & 0 & 274 & 2834 \\ 64 & 0 & 3137 & 57 \end{pmatrix}$
Transition probability	$M_{(0.7\mu\text{M})} = \begin{pmatrix} 0.9557 & 0.0263 & 0 & 0.0179 \\ 0.6206 & 0 & 0 & 0.3794 \\ 0.0695 & 0 & 0.0820 & 0.8485 \\ 0.0196 & 0 & 0.9629 & 0.0175 \end{pmatrix}$
Probability of the four states	$P_{(0.7\mu\text{M})} = (0.6079 \quad 0.0160 \quad 0.1925 \quad 0.1835)$
Asymmetric matrix	$C_{(0.7\mu\text{M})} = \begin{pmatrix} 0 & 0.0030 & -0.0067 & 0.0036 \\ -0.0030 & 0 & 0 & 0.0030 \\ 0.0067 & 0 & 0 & -0.0067 \\ -0.0036 & -0.0030 & 0.0067 & 0 \end{pmatrix}$
Symmetric matrix	$D_{(0.7\mu\text{M})} = \begin{pmatrix} 0.5810 & 0.0130 & 0.0067 & 0.0073 \\ 0.0130 & 0 & 0 & 0.0030 \\ 0.0067 & 0 & 0.0158 & 0.1700 \\ 0.0073 & 0.0030 & 0.1700 & 0.0032 \end{pmatrix}$
Net fluxes value	$J_{(0.7\mu\text{M})} = \begin{pmatrix} J_1(\text{state1, state2, state3, state1}) = 0.0061 \\ J_2(\text{state1, state4, state3, state1}) = 0.0073 \\ J_3(\text{state2, state4, state3, state2}) = 0.0061 \end{pmatrix}$

Following the master equation, parameters of net flux are determined by fitting the real-time trajectories of cell morphology at 0.7  $\mu\text{M}$  to hidden Markov chain models.

Related to [Figure 6E](#).

## DISCUSSION

In this study, we quantitatively uncovered and interpreted the yeast cell fate decision-making in response to pheromone using biological and physical methods. Using flow cytometry, we examined the induction of yeast cells by different concentrations of pheromone to determine the critical threshold for eliciting a cellular response. The purpose of the fitting curve in [Figure 2A](#) was to estimate the pheromone dose by determining at what concentration the expression of Fus3 exhibited double peaks. Continuous microscopy observations of *FUS3*-GFP strain yeast cells provided us with a microscopic and mesoscopic view of how the cells responded to pheromone. The four stages of Fus3 expression

**Table 6. The quantitative parameters in the net flux theory**

Pheromone dose ( $\mu\text{M}$ )	0.8
Number of transitions	$N_{(0.8\mu\text{M})} = \begin{pmatrix} 11957 & 328 & 0 & 140 \\ 218 & 4427 & 0 & 101 \\ 52 & 34 & 584 & 68 \\ 131 & 6 & 167 & 6 \end{pmatrix}$
Transition probability	$M_{(0.8\mu\text{M})} = \begin{pmatrix} 0.9623 & 0.0264 & 0 & 0.0113 \\ 0.0459 & 0.9328 & 0 & 0.0213 \\ 0.0705 & 0.0461 & 0.7913 & 0.0921 \\ 0.4226 & 0.0194 & 0.5387 & 0.0194 \end{pmatrix}$
Probability of the four states	$P_{(0.8\mu\text{M})} = (0.6447 \quad 0.2905 \quad 0.0467 \quad 0.0181)$
Asymmetric matrix	$C_{(0.8\mu\text{M})} = \begin{pmatrix} 0 & 0.0018 & -0.0016 & -0.0002 \\ -0.0018 & 0 & -0.0011 & 0.0029 \\ 0.0016 & 0.0011 & 0 & -0.0027 \\ 0.0002 & -0.0029 & 0.0027 & 0 \end{pmatrix}$
Symmetric matrix	$D_{(0.8\mu\text{M})} = \begin{pmatrix} 0.6204 & 0.0152 & 0.0016 & 0.0075 \\ 0.0152 & 0.2709 & 0.0011 & 0.0033 \\ 0.0016 & 0.0011 & 0.0370 & 0.0070 \\ 0.0075 & 0.0033 & 0.0070 & 0.0004 \end{pmatrix}$
Net fluxes value	$J_{(0.8\mu\text{M})} = \begin{pmatrix} J_1(\text{state1, state2, state3, state1}) = 0.0037 \\ J_2(\text{state1, state4, state3, state1}) = -0.0004 \\ J_3(\text{state2, state4, state3, state2}) = 0.0058 \end{pmatrix}$

Following the master equation, parameters of net flux are determined by fitting the real-time trajectories of cell morphology at 0.8  $\mu\text{M}$  to hidden Markov chain models.

Related to [Figure 6E](#).

**Table 7. The quantitative parameters in the net flux theory**

Pheromone dose ( $\mu\text{M}$ )	1.0
Number of transitions	$N_{(1.0\mu\text{M})} = \begin{pmatrix} 61 & 0 & 10956 & 41 \\ 0 & 0 & 24 & 0 \\ 10989 & 0 & 338 & 0 \\ 11 & 24 & 0 & 380 \end{pmatrix}$
Transition probability	$M_{(1.0\mu\text{M})} = \begin{pmatrix} 0.0055 & 0 & 0.9908 & 0.0037 \\ 0 & 0 & 1.0000 & 0 \\ 0.9702 & 0 & 0.0298 & 0 \\ 0.0265 & 0.0578 & 0 & 0.9157 \end{pmatrix}$
Probability of the four states	$P_{(1.0\mu\text{M})} = (0.4830 \quad 0.0012 \quad 0.4945 \quad 0.0212)$
Asymmetric matrix	$C_{(1.0\mu\text{M})} = 1.0e - 03 * \begin{pmatrix} 0 & 0 & -0.6140 & 0.6140 \\ 0 & 0 & 0.6140 & -0.6140 \\ 0.6140 & -0.6140 & 0 & 0 \\ -0.6140 & 0.6140 & 0 & 0 \end{pmatrix}$
Symmetric matrix	$D_{(1.0\mu\text{M})} = \begin{pmatrix} 0.0027 & 0 & 0.4792 & 0.0012 \\ 0 & 0 & 0.0006 & 0.0006 \\ 0.4792 & 0.0006 & 0.0148 & 0 \\ 0.0012 & 0.0006 & 0 & 0.0194 \end{pmatrix}$
Net fluxes value	$J_{(1.0\mu\text{M})} = \begin{pmatrix} J_1(\text{state1, state2, state3, state1}) = 0.0000 \\ J_2(\text{state1, state4, state3, state1}) = -0.0012 \\ J_3(\text{state2, state4, state3, state2}) = -0.0012 \end{pmatrix}$

Following the master equation, parameters of net flux are determined by fitting the real-time trajectories of cell morphology at 1.0  $\mu\text{M}$  to hidden Markov chain models.

Related to [Figure 6E](#).

levels at a 0.7  $\mu\text{M}$  pheromone concentration accurately depicted the mesoscopic cell behavior of cell-cycle arrest and polar growth ([Figure 2B](#)). Among them, the Fus3 expression levels in the stable stage (b2–b3) fluctuate around a fixed value, which was considered a non-equilibrium steady-state period. As our subsequent analysis centered on the non-equilibrium steady-state phase, we chose five pheromone concentrations as stimuli that allowed the yeast cells to maintain a stable-state phase for a sufficient amount of time.

To explore the fate of Fus3 gene expression in a non-equilibrium steady state, we chose data that, after 600 min, brought all the cell fluorescence trajectories into stable-state phase ([Figure 3A](#)). The two fates of Fus3 that resulted from cellular decision-making were separated by the Markov fitting of the trajectories ([Figure 3B](#)). The criterion for data fitting is the probability that the fluorescence intensity at a particular moment in the trajectory belonged to a high state ( $H_H, H_O$ ) or a low state ( $L_L, L_O$ ) multiplied by their respective transition probabilities

**Table 8. The quantitative parameters in the net flux theory**

Pheromone dose ( $\mu\text{M}$ )	2.0
Number of transitions	$N_{(2.0\mu\text{M})} = \begin{pmatrix} 67 & 0 & 0 & 1 \\ 2 & 96 & 59 & 2212 \\ 0 & 7 & 31075 & 474 \\ 0 & 2284 & 382 & 1 \end{pmatrix}$
Transition probability	$M_{(2.0\mu\text{M})} = \begin{pmatrix} 0.9853 & 0 & 0 & 0.0147 \\ 0.0008 & 0.0405 & 0.0249 & 0.9337 \\ 0 & 0.0002 & 0.9848 & 0.0150 \\ 0 & 0.8564 & 0.1432 & 0.0004 \end{pmatrix}$
Probability of the four states	$P_{(2.0\mu\text{M})} = (0.0040 \quad 0.0699 \quad 0.8480 \quad 0.0781)$
Asymmetric matrix	$C_{(2.0\mu\text{M})} = 1.0e - 03 * \begin{pmatrix} 0 & -0.0295 & 0 & 0.0295 \\ 0.0295 & 0 & 0.7763 & -0.8058 \\ 0 & -0.7763 & 0 & 0.7763 \\ -0.0295 & 0.8058 & -0.7763 & 0 \end{pmatrix}$
Symmetric matrix	$D_{(2.0\mu\text{M})} = \begin{pmatrix} 0.0040 & 0.0000 & 0 & 0.0000 \\ 0.0000 & 0.0028 & 0.0010 & 0.0661 \\ 0 & 0.0010 & 0.8351 & 0.0120 \\ 0.0000 & 0.0661 & 0.0120 & 0.0000 \end{pmatrix}$
Net fluxes value	$J_{(2.0\mu\text{M})} = \begin{pmatrix} J_1(\text{state1, state2, state3, state1}) = -0.0001 \\ J_2(\text{state1, state4, state3, state1}) = -0.0001 \\ J_3(\text{state2, state4, state3, state2}) = -0.0016 \end{pmatrix}$

Following the master equation, parameters of net flux are determined by fitting the real-time trajectories of cell morphology at 2.0  $\mu\text{M}$  to hidden Markov chain models.

Related to [Figure 6E](#).

**Table 9. The quantitative parameters in the net flux theory**

Pheromone dose ( $\mu\text{M}$ )	3.0
Number of transitions	$N_{(3.0\mu\text{M})} = \begin{pmatrix} 0 & 0 & 0 & 870 \\ 0 & 13609 & 48 & 296 \\ 861 & 286 & 0 & 471 \\ 9 & 1 & 1628 & 48 \end{pmatrix}$
Transition probability	$M_{(3.0\mu\text{M})} = \begin{pmatrix} 0 & 0 & 0 & 1.0000 \\ 0 & 0.9753 & 0.0034 & 0.0212 \\ 0.5321 & 0.1768 & 0 & 0.2911 \\ 0.0053 & 0.0006 & 0.9656 & 0.0285 \end{pmatrix}$
Probability of the four states	$P_{(3.0\mu\text{M})} = (0.0552 \quad 0.7385 \quad 0.1027 \quad 0.1037)$
Asymmetric matrix	$C_{(3.0\mu\text{M})} = \begin{pmatrix} 0 & 0 & -0.0273 & 0.0273 \\ 0 & 0 & -0.0078 & 0.0078 \\ 0.0273 & 0.0078 & 0 & -0.0351 \\ -0.0273 & -0.0078 & 0.0351 & 0 \end{pmatrix}$
Symmetric matrix	$D_{(3.0\mu\text{M})} = \begin{pmatrix} 0 & 0 & 0.0273 & 0.0279 \\ 0 & 0.7203 & 0.0103 & 0.0079 \\ 0.0273 & 0.0103 & 0 & 0.0650 \\ 0.0279 & 0.0079 & 0.0650 & 0.0030 \end{pmatrix}$
Net fluxes value	$J_{(3.0\mu\text{M})} = \begin{pmatrix} J_1(\text{state1, state2, state3, state1}) = -0.0000 \\ J_2(\text{state1, state4, state3, state1}) = 0.0546 \\ J_3(\text{state2, state4, state3, state2}) = 0.0156 \end{pmatrix}$

Following the master equation, parameters of net flux are determined by fitting the real-time trajectories of cell morphology at 3.0  $\mu\text{M}$  to hidden Markov chain models.

Related to [Figure 6E](#).

([Figure 3E](#)). Consequently, there was a chance that the value of the fluorescence intensity in the low state was greater than the value of the fluorescence intensity in the high state. We proposed that the two fates of Fus3 expressions observed in signaling were explained by a logical sequence of point-to-point feedback regulation between proteins. Notably, even though the protein-to-protein feedback regulation described previously had been validated by previous biological experiments,<sup>77–81,86–95</sup> our claims focused primarily on establishing a dynamical logical connection between these isolated regulatory processes from a global perspective. For the purpose of validating this dynamic molecular mechanism, one may wonder why the ( $L_1, H_0$ ) and ( $H_1, L_0$ ) states did not appear in this scheme. We know from experimental evidence that the absence of the ( $L_1, H_0$ ) and ( $H_1, L_0$ ) states was due to the strong correlation between intra- and extra-nuclear fluorescence intensities. If the four fates emerge on the landscape of intra- and extra-nuclear fluorescence intensities of Fus3, the Pearson correlation coefficient between these two types of trajectories would be zero.<sup>110</sup> Moreover, the feedback model of forward activation and negative inhibition favored the formation of two states from a physical standpoint ([Figure 3D](#)).

Between steady states, the cellular decision-making is primarily reflected by the transition rate, transition probability, residence time, and potential barrier height. Due to the relative nature of the high and low states at each pheromone concentration, their physical characteristics can be compared directly, but not at different concentrations. To compare the relative significance of these physical characteristics at different concentrations, a similar normalized approach (high/low) was used. At 0.7–0.8  $\mu\text{M}$ , a slight increase in barrier height significantly lengthened the residence time of the high state. At 1.0–3.0  $\mu\text{M}$ , the residence time also decreased gradually as the barrier height decreased ([Figure 4D](#)). In our biological system, the positive correlation statement regarding barrier height and residence time was confirmed ([Figure 4C](#)). Certainly, such physical characteristics that quantify cellular decision-making have significant biological implications for the study of yeast response behavior. Positive feedback regulation in the gene network (“Pheromone  $\rightarrow$  Fus3” and “Fus3  $\rightarrow$  Fus3”), for example, increased the potential barrier height on the gene expression landscape, whereas negative feedback regulation decreased it ( $l_1, l_2$ ) ([Figures 1](#) and [3C](#)). The residence time at various pheromone concentrations revealed which gene expression fate yeast cells preferred in response to the pheromone.

Some studies believe that the establishment of polarity helps organisms to survive better in nature.<sup>111,112</sup> Due to the inability of yeast’s chemotactic response to swim as that of *E. coli*, its polar growth could only grow in the direction of a high concentration of pheromone, achieving mutual contact and fusion between heterothallic yeasts 2,4,25. To quantify the mesoscopic behavior of yeast cells in polar growth, which grew and stopped intermittently, the yeast cells were characterized as a combination of filled circles. The white edge of the yeast cell image was the cell wall ([Figure 5A](#)). Therefore, the cell-filling circles were based on the outermost edge of the cell wall as the cell boundary. Rather than using the cell area, the total length, or the arithmetic mean of the length, we chose to describe the cell morphology using the reciprocal of the radius in the cell-filled circle multiplied by the number of filled circles, i.e.,  $H_n = n \left( \frac{1}{R_1} + \frac{1}{R_2} + \dots + \frac{1}{R_n} \right)$ . This method has the following advantages: first, it could reflect the deformation of different parts of the cell; and second,  $H_n$  is a statistic that can reflect both the process and outcome of the cell polarity growth. It was important to note that when a cell grew laterally, its length also increased, so the terms lateral growth and longitudinal growth were relative rather than absolute descriptions of length and width.

The cell growth rate primarily characterized the process of cell polar growth, whereas the cell morphology primarily characterized the outcome. Specifically, the cell growth rate is actually the cell deformation rate. To verify the molecular mechanism of the growth rate for directional (model L) and non-directional (model W) growth, we constructed a dual-fluorescence system (CDC24-GFP\_FUS3-RFP) to demonstrate

that there was a time lag in the multi-level protein signaling behavior. Due to the different maturation times of the two fluorescent proteins (GFP and RFP), the lag time between Fus3 and Cdc24 was only a relative quantity. Nonetheless, the delay time of the dual-fluorescence system at different positions was used to quantify the practical significance of multipolar signal transduction. Notably, the non-directional growth (model W:  $P_2$ ) did not consist solely of the polar growth pathway of  $P_2$ , but rather a relative weight simplification to differentiate it from the directional growth (model L:  $P_1 + P_2$ ). To confirm that the fast growth rate (model F) and slow growth rate (model S) corresponded to the high and low states of Fus3, we explored the association between growth rates and dual-fluorescent gene expression states. The high state ( $H_1, H_0$ ) was primarily included in the fast growth rate, whereas the low state ( $L_1, L_0$ ) was primarily included in the slow growth rate, confirming the molecular mechanism of F and S (Figures 5H and Table 3). In addition, there must be a lag between the expression of Fus3p and the observed cell growth, resulting in a low fluorescence state during fast cell growth and a high fluorescence state during slow cell growth.

For statistical analysis of different cell morphologies, we distinguished four cell morphological fates roughly as  $F_1$ – $F_4$  to provide a more intuitive description (Figure 6A). Nevertheless, the division of actual cell morphological fate was determined by fitting the trajectories, and not arbitrarily by the size of  $H_n$ . Given that  $H_n$  is extremely sensitive to changes in length and width in different parts of the cell, the area of cells that were morphologically divided into the four categories did not differ significantly from their overall appearance (Figure 6B). Our justification for proposing the molecular mechanisms of the four cell morphological fates is that morphology is the accumulation of a growth process. Due to the fact that the cell morphology described by  $H_n$  resembled the relative length and width of a cell, the capacity to grow in both directions can explain the emergence of cell morphologies (Figure 6C). In addition, in the statistical graph of cell morphology, other fates tended to disappear, with the exception of the increase in the proportion of  $F_2$ . This indicated that the intracellular phase transition trend occurred at 3.0  $\mu\text{M}$  as a result of enhanced negative feedback regulation ( $I_2$  in Figure 1). The coordinates of the cell morphology statistics chart at 3.0  $\mu\text{M}$  were deviated from those of other concentrations due to the phase transition trend in the system, which altered the measurement scale of the four morphological fates. To explain the physics of the phase transitions in the biological system, we quantified the degree to which the detailed balance collapsed by employing the net flux characterizing the non-equilibrium statistical physics. The results demonstrated that the non-equilibrium dynamics of the biological system was supported by the significant increase in net flux of the morphological system at high pheromone dose (3.0  $\mu\text{M}$ ), causing the instability and phase transition.

Finally, we developed a simplified model of the gene regulatory network for signal transduction in order to confirm the global rationality of the dynamic sequential mechanism. Thus far, we have established the logical links between the functions of regulated proteins in the pheromone pathway for mating through the underlying signal transduction process. While our validation method differs from the conventional approach of constructing yeast mutants, it has been successful in observing realistic cellular response behavior. Our future research will focus on utilizing fluorescent labels to enable real-time visualization of the dynamics of signaling pathways. Specifically, we plan to construct a multi-dimensional fluorescent system to elucidate the temporal and spatial dynamics of cellular responses, including potential crosstalk between different signaling pathways. This approach will provide a more comprehensive and quantitative understanding of how cells respond to various stimuli, and how these responses are integrated at the molecular level. Furthermore, we will explore how pheromone modulates cell fate dynamics by regulating the depth of basins on the landscape, as analogous modulation of a transcriptional parameter was shown to impact cell state transitions.<sup>13</sup> These future investigations will establish a more thorough characterization and mechanistic understanding of cell fate decision dynamics.

### Limitations of the study

There are some potential limitations in the current study. First, due to the technical constraints on real-time tracking in live cells, we could not distinguish phosphorylated Fus3 and unphosphorylated Fus3p *in vivo*, nor quantify the amount of Fus3p involved in specific biochemical reactions. Only the total amount of Fus3 was observed as a proxy. Second, experimental variations could arise if different batches of pheromone were used, as minor differences in pheromone purity and stability may affect the induced responses. Thus, experiments for each concentration were preferably performed using pheromone solutions prepared in the same batch. Third, larger sample sizes could facilitate building a more comprehensive landscape model that captures the global dynamics. Future investigations with improved technical capabilities, tighter experimental controls, and larger datasets are warranted to address these limitations and gain a deeper mechanistic understanding of the signaling systems.

### STAR★METHODS

Detailed methods are provided in the online version of this paper and include the following:

- KEY RESOURCE STABLE
- RESOURCE AVAILABILITY
  - Lead contact
  - Materials availability
  - Data and code availability
- EXPERIMENTAL MODEL AND SUBJECT DETAILS
  - Yeast strain
- METHOD DETAILS
  - Preparation of pheromone culture medium

- Flow cytometry analysis
- Microfluidic platform for yeast cell cultivation and operational procedure
- Microscopy measurements
- Basis of fluorescent protein and interval choices
- Background signal processing
- Data collection and sample sizes
- Estimation of uncertainty and interpretation of results
- Dual fluorescence system construction
- Quantifying fluorescent tag photobleaching
- Real time image analysis
- Steady-state image analysis
- Cell fate identification using Hidden Markov Model
- Distinguishing the boundaries of the nucleus
- Filled circle model in cell shape
- Characterizing the deformation behavior of yeast cells
- Derivation of the transition rates
- Calculating residence and switching times in multi-stable systems
- The statistical physics connection between cell state switching and residence time
- Unraveling the interplay of duration, pheromone concentration, and cell state switching
- Decomposing of the flux in the cell morphology
- Gillespie algorithm-based simulation
- The comprehensive description of the biochemical reactions in stochastic simulations
- **QUANTIFICATION AND STATISTICAL ANALYSIS**

## SUPPLEMENTAL INFORMATION

Supplemental information can be found online at <https://doi.org/10.1016/j.isci.2023.107885>.

## ACKNOWLEDGMENTS

S.L., Q.L., and E.W. acknowledge the support of the National Key R&D Program of China (2020YFB2009004) and the National Natural Science Foundation of China with Grant No. 21721003.

## AUTHOR CONTRIBUTIONS

Conceptualization: S.L., Q.L., and J.W.; methodology: S.L., Q.L., E.W., and J.W.; investigation: S.L. and Q.L.; visualization: S.L., Q.L., and J.W.; project administration and supervision: E.W. and J.W.; writing – original draft: S.L., Q.L., and J.W.; writing review & editing: S.L. and J.W.

## DECLARATION OF INTERESTS

The authors declare no competing interests.

## INCLUSION AND DIVERSITY

We support inclusive, diverse, and equitable conduct of research.

Received: May 23, 2023

Revised: August 9, 2023

Accepted: September 7, 2023

Published: September 9, 2023

## REFERENCES

1. Berg, H.C., and Brown, D.A. (1972). Chemotaxis in *Escherichia coli* analysed by three-dimensional tracking. *Nature* 239, 500–504.
2. Macnab, R.M., and Koshland, D.E., Jr. (1972). The gradient-sensing mechanism in bacterial chemotaxis. *Proc. Natl. Acad. Sci. USA* 69, 2509–2512.
3. Yuan, J., Fahmer, K.A., Turner, L., and Berg, H.C. (2010). Asymmetry in the clockwise and counterclockwise rotation of the bacterial flagellar motor. *Proc. Natl. Acad. Sci. USA* 107, 12846–12849.
4. Sourjik, V., and Wingreen, N.S. (2012). Responding to chemical gradients: bacterial chemotaxis. *Curr. Opin. Cell Biol.* 24, 262–268.
5. De Oliveira, S., Rosowski, E.E., and Huttenlocher, A. (2016). Neutrophil migration in infection and wound repair: going forward in reverse. *Nat. Rev. Immunol.* 16, 378–391.
6. Zhou, P., Gao, X., Li, X., Li, L., Niu, C., Ouyang, Q., Lou, H., Li, T., and Li, F. (2021). Stochasticity triggers activation of the s-phase checkpoint pathway in budding yeast. *Phys. Rev. X* 11, 011004.
7. Fu, B., Sengupta, K., Genova, L.A., Santiago, A.G., Jung, W., Krzemiński, Ł., Chakraborty, U.K., Zhang, W., and Chen, P. (2020). Metal-

- induced sensor mobilization turns on affinity to activate regulator for metal detoxification in live bacteria. *Proc. Natl. Acad. Sci. USA* 117, 13248–13255.
8. Slessareva, J.E., and Dohlman, H.G. (2006). G protein signaling in yeast: new components, new connections, new compartments. *Science* 314, 1412–1413.
  9. Chen, R.E., and Thorner, J. (2007). Function and regulation in MAPK signaling pathways: lessons learned from the yeast *Saccharomyces cerevisiae*. *Biochim. Biophys. Acta* 1773, 1311–1340.
  10. Wang, Y., and Dohlman, H.G. (2004). Pheromone signaling mechanisms in yeast: a prototypical sex machine. *Science* 306, 1508–1509.
  11. Gustin, M.C., Albertyn, J., Alexander, M., and Davenport, K. (1998). MAP kinase pathways in the yeast *Saccharomyces cerevisiae*. *Microbiol. Mol. Biol. Rev.* 62, 1264–1300.
  12. Herskowitz, I. (1988). Life cycle of the budding yeast *Saccharomyces cerevisiae*. *Microbiol. Rev.* 52, 536–553.
  13. Hull, C.M., Raisner, R.M., and Johnson, A.D. (2000). Evidence for mating of the "asexual" yeast *Candida albicans* in a mammalian host. *Science* 289, 307–310.
  14. Warringer, J., Zörgö, E., Cubillos, F.A., Zia, A., Gjuvsland, A., Simpson, J.T., Forsmark, A., Durbin, R., Omholt, S.W., Louis, E.J., et al. (2011). Trait variation in yeast is defined by population history. *PLoS Genet.* 7, e1002111.
  15. Zörgö, E., Chwialkowska, K., Gjuvsland, A.B., Garré, E., Sunnerhagen, P., Liti, G., Blomberg, A., Omholt, S.W., and Warringer, J. (2013). Ancient evolutionary trade-offs between yeast ploidy states. *PLoS Genet.* 9, e1003388.
  16. Norris, D., and Osley, M.A. (1987). The two gene pairs encoding H2A and H2B play different roles in the *Saccharomyces cerevisiae* life cycle. *Mol. Cell Biol.*
  17. Haber, J.E. (2012). Mating-type genes and MAT switching in *Saccharomyces cerevisiae*. *Genetics* 191, 33–64.
  18. Bao, M.Z., Schwartz, M.A., Cantin, G.T., Yates, J.R., III, and Madhani, H.D. (2004). Pheromone-dependent destruction of the Tec1 transcription factor is required for MAP kinase signaling specificity in yeast. *Cell* 119, 991–1000.
  19. Jenness, D.D., Burkholder, A.C., and Hartwell, L.H. (1983). Binding of  $\alpha$ -factor pheromone to yeast cells: chemical and genetic evidence for an  $\alpha$ -factor receptor. *Cell* 35, 521–529.
  20. Youk, H., and Lim, W.A. (2014). Secreting and sensing the same molecule allows cells to achieve versatile social behaviors. *Science* 343, 1242782.
  21. Rose, M.D. (1996). Nuclear fusion in the yeast *Saccharomyces cerevisiae*. *Annu. Rev. Cell Dev. Biol.* 12, 663–695.
  22. White, J.M., and Rose, M.D. (2001). Yeast mating: getting close to membrane merger. *Curr. Biol.* 11, R16–R20.
  23. Molk, J.N., and Bloom, K. (2006). Microtubule dynamics in the budding yeast mating pathway. *J. Cell Sci.* 119, 3485–3490.
  24. Bardwell, L. (2005). A walk-through of the yeast mating pheromone response pathway. *Peptides* 26, 339–350.
  25. Neiman, A.M., and Herskowitz, I. (1994). Reconstitution of a yeast protein kinase cascade in vitro: activation of the yeast MEK homologue STE7 by STE11. *Proc. Natl. Acad. Sci. USA* 91, 3398–3402.
  26. Errede, B., Gartner, A., Zhou, Z., Nasmyth, K., and Ammerer, G. (1993). MAP kinase-related FUS3 from *S. cerevisiae* is activated by STE7 in vitro. *Nature* 362, 261–264.
  27. Butty, A.C., Pryciak, P.M., Huang, L.S., Herskowitz, I., and Peter, M. (1998). The Role of Far1p in Linking the Heterotrimeric G Protein to Polarity Establishment Proteins During Yeast Mating. *Science* 282, 1511–1516.
  28. Matheos, D., Metodiev, M., Muller, E., Stone, D., and Rose, M.D. (2004). Pheromone-induced polarization is dependent on the Fus3p MAPK acting through the formin Bni1p. *J. Cell Biol.* 165, 99–109.
  29. Peter, M., Gartner, A., Horecka, J., Ammerer, G., and Herskowitz, I. (1993). FAR1 links the signal transduction pathway to the cell cycle machinery in yeast. *Cell* 73, 747–760.
  30. Elion, E.A., Satterberg, B., and Kranz, J.E. (1993). FUS3 phosphorylates multiple components of the mating signal transduction cascade: evidence for STE12 and FAR1. *Mol. Biol. Cell* 4, 495–510.
  31. Roberts, R.L., and Fink, G.R. (1994). Elements of a single MAP kinase cascade in *Saccharomyces cerevisiae* mediate two developmental programs in the same cell type: mating and invasive growth. *Genes Dev.* 8, 2974–2985.
  32. Herskowitz, I. (1995). MAP kinase pathways in yeast: for mating and more. *Cell* 80, 187–197.
  33. Elion, E.A., Brill, J.A., and Fink, G.R. (1991). FUS3 represses CLN1 and CLN2 and in concert with KSS1 promotes signal transduction. *Proc. Natl. Acad. Sci. USA* 88, 9392–9396.
  34. Blackwell, E., Halatek, I.M., Kim, H.-J.N., Ellicott, A.T., Obukhov, A.A., and Stone, D.E. (2003). Effect of the pheromone-responsive G $\alpha$  and phosphatase proteins of *Saccharomyces cerevisiae* on the subcellular localization of the Fus3 mitogen-activated protein kinase. *Mol. Cell Biol.* 23, 1135–1150.
  35. van Drogen, F., Stucke, V.M., Jorritsma, G., and Peter, M. (2001). MAP kinase dynamics in response to pheromones in budding yeast. *Nat. Cell Biol.* 3, 1051–1059.
  36. Chang, F., and Herskowitz, I. (1990). Identification of a gene necessary for cell cycle arrest by a negative growth factor of yeast: FAR1 is an inhibitor of a G1 cyclin. *CLN2. Cell* 63, 999–1011.
  37. Shimada, Y., Gulli, M.-P., and Peter, M. (2000). Nuclear sequestration of the exchange factor Cdc24 by Far1 regulates cell polarity during yeast mating. *Nat. Cell Biol.* 2, 117–124.
  38. Segall, J.E. (1993). Polarization of yeast cells in spatial gradients of alpha mating factor. *Proc. Natl. Acad. Sci. USA* 90, 8332–8336.
  39. Takizawa, P.A., Sil, A., Swedlow, J.R., Herskowitz, I., and Vale, R.D. (1997). Actin-dependent localization of an RNA encoding a cell-fate determinant in yeast. *Nature* 389, 90–93.
  40. Colman-Lerner, A., Gordon, A., Serra, E., Chin, T., Resnekov, O., Endy, D., Pesce, C.G., and Brent, R. (2005). Regulated cell-to-cell variation in a cell-fate decision system. *Nature* 437, 699–706.
  41. Weinberger, L.S., Burnett, J.C., Toettcher, J.E., Arkin, A.P., and Schaffer, D.V. (2005). Stochastic gene expression in a lentiviral positive-feedback loop: HIV-1 Tat fluctuations drive phenotypic diversity. *Cell* 122, 169–182.
  42. Choi, P.J., Cai, L., Frieda, K., and Xie, X.S. (2008). A stochastic single-molecule event triggers phenotype switching of a bacterial cell. *Science* 322, 442–446.
  43. St-Pierre, F., and Endy, D. (2008). Determination of cell fate selection during phage lambda infection. *Proc. Natl. Acad. Sci. USA* 105, 20705–20710.
  44. Zeng, L., Skinner, S.O., Zong, C., Sippy, J., Feiss, M., and Golding, I. (2010). Decision making at a subcellular level determines the outcome of bacteriophage infection. *Cell* 141, 682–691.
  45. Gordley, R.M., Williams, R.E., Bashor, C.J., Toettcher, J.E., Yan, S., and Lim, W.A. (2016). Engineering dynamical control of cell fate switching using synthetic phosphoregulators. *Proc. Natl. Acad. Sci. USA* 113, 13528–13533.
  46. Fang, X., Liu, Q., Bohrer, C., Hensel, Z., Han, W., Wang, J., and Xiao, J. (2018). Cell fate potentials and switching kinetics uncovered in a classic bistable genetic switch. *Nat. Commun.* 9, 2787.
  47. Jiang, Z., Tian, L., Fang, X., Zhang, K., Liu, Q., Dong, Q., Wang, E., and Wang, J. (2019). The emergence of the two cell fates and their associated switching for a negative auto-regulating gene. *BMC Biol.* 17, 49.
  48. Wang, W., Douglas, D., Zhang, J., Kumari, S., Enuameh, M.S., Dai, Y., Wallace, C.T., Watkins, S.C., Shu, W., and Xing, J. (2020). Live-cell imaging and analysis reveal cell phenotypic transition dynamics inherently missing in snapshot data. *Sci. Adv.* 6, eaba9319.
  49. Yosef, N., and Regev, A. (2011). Impulse control: temporal dynamics in gene transcription. *Cell* 144, 886–896.
  50. Bar-Joseph, Z., Gitter, A., and Simon, I. (2012). Studying and modelling dynamic biological processes using time-series gene expression data. *Nat. Rev. Genet.* 13, 552–564.
  51. Doncic, A., Atay, O., Valk, E., Grande, A., Bush, A., Vasen, G., Colman-Lerner, A., Loog, M., and Skotheim, J.M. (2015). Compartmentalization of a bistable switch enables memory to cross a feedback-driven transition. *Cell* 160, 1182–1195.
  52. Hasty, J., McMillen, D., Isaacs, F., and Collins, J.J. (2001). Computational studies of gene regulatory networks: in numero molecular biology. *Nat. Rev. Genet.* 2, 268–279.
  53. Behar, M., Hao, N., Dohlman, H.G., and Elston, T.C. (2008). Dose-to-duration encoding and signaling beyond saturation in intracellular signaling networks. *PLoS Comput. Biol.* 4, e1000197.
  54. Wang, W., Li, G.-W., Chen, C., Xie, X.S., and Zhuang, X. (2011). Chromosome organization by a nucleoid-associated protein in live bacteria. *Science* 333, 1445–1449.
  55. Caudron, F., and Barral, Y. (2013). A super-assembly of Whi3 encodes memory of deceptive encounters by single cells during yeast courtship. *Cell* 155, 1244–1257.
  56. Weinberg, J.S., and Drubin, D.G. (2014). Regulation of clathrin-mediated endocytosis by dynamic ubiquitination and deubiquitination. *Curr. Biol.* 24, 951–959.
  57. Conlon, P., Gelin-Licht, R., Ganesan, A., Zhang, J., and Levchenko, A. (2016). Single-cell dynamics and variability of MAPK

- activity in a yeast differentiation pathway. *Proc. Natl. Acad. Sci. USA* 113, E5896–E5905.
58. Leonetti, M.D., Sekine, S., Kamiyama, D., Weissman, J.S., and Huang, B. (2016). A scalable strategy for high-throughput GFP tagging of endogenous human proteins. *Proc. Natl. Acad. Sci. USA* 113, E3501–E3508.
  59. Özsezen, S., Papagiannakis, A., Chen, H., Niebel, B., Milias-Argetis, A., and Heinemann, M. (2019). Inference of the high-level interaction topology between the metabolic and cell-cycle oscillators from single-cell dynamics. *Cell systems* 9, 354–365.e356.
  60. Chakravarty, A.K., Smejkal, T., Itakura, A.K., Garcia, D.M., and Jarosz, D.F. (2020). A non-amyloid prion particle that activates a heritable gene expression program. *Mol. Cell* 77, 251–265.e9.
  61. Klaiaps, C.L., Gropp, M.H.M., Hipp, M.S., and Hartl, F.U. (2020). Sisl1 potentiates the stress response to protein aggregation and elevated temperature. *Nat. Commun.* 11, 6271.
  62. Mouton, S.N., Thaller, D.J., Crane, M.M., Rempel, I.L., Terpstra, O.T., Steen, A., Kaerberlein, M., Lusk, C.P., Boersma, A.J., and Veenhoff, L.M. (2020). A physicochemical perspective of aging from single-cell analysis of pH, macromolecular and organellar crowding in yeast. *Elife* 9, e54707.
  63. Ptak, C., Saik, N.O., Premashankar, A., Lapetina, D.L., Aitchison, J.D., Montpetit, B., and Wozniak, R.W. (2021). Phosphorylation-dependent mitotic SUMOylation drives nuclear envelope–chromatin interactions. *J. Cell Biol.* 220, e202103036.
  64. Chaturvedi, S., Pablo, M., Wolf, M., Rosas-Rivera, D., Calia, G., Kumar, A.J., Vardi, N., Du, K., Glazier, J., Ke, R., et al. (2022). Disrupting autorepression circuitry generates “open-loop lethality” to yield escape-resistant antiviral agents. *Cell* 185, 2086–2102.e22.
  65. Feng, W., Argüello-Miranda, O., Qian, S., and Wang, F. (2022). Cdc14 spatiotemporally dephosphorylates Atg13 to activate autophagy during meiotic divisions. *J. Cell Biol.* 221, e202107151.
  66. Pinheiro, S., Pandey, S., and Pelet, S. (2022). Cellular heterogeneity: Yeast-side story. *Fungal Biol. Rev.* 39, 34–45.
  67. Davidson, E.H., and Erwin, D.H. (2006). Gene regulatory networks and the evolution of animal body plans. *Science* 311, 796–800.
  68. Wang, J., Xu, L., and Wang, E. (2008). Potential landscape and flux framework of nonequilibrium networks: Robustness, dissipation, and coherence of biochemical oscillations. *Proc. Natl. Acad. Sci. USA* 105, 12271–12276.
  69. Wang, J., Zhang, K., and Wang, E. (2008). Robustness and dissipation of mitogen-activated protein kinases signal transduction network: Underlying funneled landscape against stochastic fluctuations. *J. Chem. Phys.* 129, 135101.
  70. Wang, J., Li, C., and Wang, E. (2010). Potential and flux landscapes quantify the stability and robustness of budding yeast cell cycle network. *Proc. Natl. Acad. Sci. USA* 107, 8195–8200.
  71. Wang, J., Zhang, K., and Wang, E. (2010). Kinetic paths, time scale, and underlying landscapes: A path integral framework to study global natures of nonequilibrium systems and networks. *J. Chem. Phys.* 133, 125103.
  72. Balázs, G., Van Oudenaarden, A., and Collins, J.J. (2011). Cellular decision making and biological noise: from microbes to mammals. *Cell* 144, 910–925.
  73. Feng, H., and Wang, J. (2011). Potential and flux decomposition for dynamical systems and non-equilibrium thermodynamics: Curvature, gauge field, and generalized fluctuation-dissipation theorem. *J. Chem. Phys.* 135, 234511.
  74. Wang, J., Zhang, K., Xu, L., and Wang, E. (2011). Quantifying the Waddington landscape and biological paths for development and differentiation. *Proc. Natl. Acad. Sci. USA* 108, 8257–8262.
  75. Li, C., and Wang, J. (2014). Landscape and flux reveal a new global view and physical quantification of mammalian cell cycle. *Proc. Natl. Acad. Sci. USA* 111, 14130–14135.
  76. Zheng, W., Zhao, H., Mancera, E., Steinmetz, L.M., and Snyder, M. (2010). Genetic analysis of variation in transcription factor binding in yeast. *Nature* 464, 1187–1191.
  77. Anders, A., Ghosh, B., Glatter, T., and Sourjik, V. (2020). Design of a MAPK signalling cascade balances energetic cost versus accuracy of information transmission. *Nat. Commun.* 11, 3494.
  78. Dohlman, H.G., Song, J., Ma, D., Courchesne, W.E., and Thorner, J. (1996). Sst2, a negative regulator of pheromone signaling in the yeast *Saccharomyces cerevisiae*: expression, localization, and genetic interaction and physical association with Gpa1 (the G-protein  $\alpha$  subunit). *Mol. Cell Biol.* 16, 5194–5209.
  79. Hermansyah, Sugiyama, M., Kaneko, Y., and Harashima, S. (2009). Yeast protein phosphatases Ptp2p and Msg5p are involved in G1–S transition, CLN2 transcription, and vacuole morphogenesis. *Arch. Microbiol.* 191, 721–733.
  80. Laviña, W.A., Laviña, W.A., Sugiyama, M., Kaneko, Y., and Harashima, S. (2010). Identification of protein kinase disruptions as suppressors of the calcium sensitivity of *S. cerevisiae* [Delta] ptp2 [Delta] msg5 protein phosphatase double disruptant. *Arch. Microbiol.* 192, 157–165.
  81. Laviña, W.A., Sugiyama, M., Sugiyama, M., Kaneko, Y., and Harashima, S. (2013). Functionally redundant protein phosphatase PTP2 and MSG5 co-regulate the calcium signaling pathway in *Saccharomyces cerevisiae* upon exposure to high extracellular calcium concentration. *J. Biosci. Bioeng.* 115, 138–146.
  82. Butty, A.-C., Pryciak, P.M., Huang, L.S., Herskowitz, I., and Peter, M. (1998). The role of Far1p in linking the heterotrimeric G protein to polarity establishment proteins during yeast mating. *Science* 282, 1511–1516.
  83. Nern, A., and Arkowitz, R.A. (1999). A Cdc24p–Far1p–G $\beta$ y protein complex required for yeast orientation during mating. *J. Cell Biol.* 144, 1187–1202.
  84. Nern, A., and Arkowitz, R.A. (2000). Nucleocytoplasmic shuttling of the Cdc42p exchange factor Cdc24p. *J. Cell Biol.* 148, 1115–1122.
  85. Chen, E.H. (2008). *Cell Fusion: Overviews and Methods* (Springer).
  86. Szczurek, E., Gat-Viks, I., Tiurny, J., and Vingron, M. (2009). Elucidating regulatory mechanisms downstream of a signaling pathway using informative experiments. *Mol. Syst. Biol.* 5, 287.
  87. Maeder, C.I., Hink, M.A., Kinkhabwala, A., Mayr, R., Bastiaens, P.I.H., and Knop, M. (2007). Spatial regulation of Fus3 MAP kinase activity through a reaction-diffusion mechanism in yeast pheromone signalling. *Nat. Cell Biol.* 9, 1319–1326.
  88. Serrano, A., Illgen, J., Brandt, U., Thieme, N., Letz, A., Lichius, A., Read, N.D., and Fleißner, A. (2018). Spatio-temporal MAPK dynamics mediate cell behavior coordination during fungal somatic cell fusion. *J. Cell Sci.* 131, jcs213462.
  89. Kranz, J.E., Satterberg, B., and Elion, E.A. (1994). The MAP kinase Fus3 associates with and phosphorylates the upstream signaling component Ste5. *Genes Dev.* 8, 313–327.
  90. Winters, M.J., Lamson, R.E., Nakanishi, H., Neiman, A.M., and Pryciak, P.M. (2005). A membrane binding domain in the Ste5 scaffold synergizes with G $\beta$ y binding to control localization and signaling in pheromone response. *Mol. Cell* 20, 21–32.
  91. Bhattacharyya, R.P., Reményi, A., Good, M.C., Bashor, C.J., Falick, A.M., and Lim, W.A. (2006). The Ste5 scaffold allosterically modulates signaling output of the yeast mating pathway. *Science* 311, 822–826.
  92. Malleshaiah, M.K., Shahrezaei, V., Swain, P.S., and Michnick, S.W. (2010). The scaffold protein Ste5 directly controls a switch-like mating decision in yeast. *Nature* 465, 101–105.
  93. Chen, T., and Kurjan, J. (1997). *Saccharomyces cerevisiae* Mpt5p interacts with Sst2p and plays roles in pheromone sensitivity and recovery from pheromone arrest. *Mol. Cell Biol.* 17, 3429–3439.
  94. Garrison, T.R., Zhang, Y., Pausch, M., Apanovitch, D., Aebersold, R., and Dohlman, H.G. (1999). Feedback phosphorylation of an RGS protein by MAP kinase in yeast. *J. Biol. Chem.* 274, 36387–36391.
  95. Parnell, S.C., Marotti, L.A., Kiang, L., Torres, M.P., Borchers, C.H., and Dohlman, H.G. (2005). Phosphorylation of the RGS protein Sst2 by the MAP kinase Fus3 and use of Sst2 as a model to analyze determinants of substrate sequence specificity. *Biochemistry* 44, 8159–8166.
  96. Park, H.-O., and Bi, E. (2007). Central roles of small GTPases in the development of cell polarity in yeast and beyond. *Microbiol. Mol. Biol. Rev.* 71, 48–96.
  97. Moseley, J.B., and Goode, B.L. (2006). The yeast actin cytoskeleton: from cellular function to biochemical mechanism. *Microbiol. Mol. Biol. Rev.* 70, 605–645.
  98. Doncic, A., Falleur-Fettig, M., and Skotheim, J.M. (2011). Distinct interactions select and maintain a specific cell fate. *Mol. Cell* 43, 528–539.
  99. Barkai, N., Rose, M.D., and Wingreen, N.S. (1998). Protease helps yeast find mating partners. *Nature* 396, 422–423.
  100. Slaughter, B.D., Schwartz, J.W., and Li, R. (2007). Mapping dynamic protein interactions in MAP kinase signaling using live-cell fluorescence fluctuation spectroscopy and imaging. *Proc. Natl. Acad. Sci. USA* 104, 20320–20325.
  101. Elion, E.A., Qi, M., and Chen, W. (2005). Signaling specificity in yeast. *Science* 307, 687–688.
  102. Fiedler, D., Braberg, H., Mehta, M., Chechik, G., Cagny, G., Mukherjee, P., Silva, A.C., Shales, M., Collins, S.R., van Wageningen,

- S., et al. (2009). Functional organization of the *S. cerevisiae* phosphorylation network. *Cell* 136, 952–963.
103. Wang, J. (2015). Landscape and flux theory of non-equilibrium dynamical systems with application to biology. *Adv. Phys.* 64, 1–137.
104. Fang, X., Kruse, K., Lu, T., and Wang, J. (2019). Nonequilibrium physics in biology. *Rev. Mod. Phys.* 91, 045004.
105. Feng, H., Zhang, K., and Wang, J. (2014). Non-equilibrium transition state rate theory. *Chem. Sci.* 5, 3761–3769.
106. Nern, A., and Arkowitz, R.A. (2000). G proteins mediate changes in cell shape by stabilizing the axis of polarity. *Mol. Cell* 5, 853–864.
107. Gillespie, D.T. (2000). The chemical Langevin equation. *J. Chem. Phys.* 113, 297–306.
108. De Jong, H. (2002). Modeling and simulation of genetic regulatory systems: a literature review. *J. Comput. Biol.* 9, 67–103.
109. Gillespie, D.T. (2001). Approximate accelerated stochastic simulation of chemically reacting systems. *J. Chem. Phys.* 115, 1716–1733.
110. Rodgers, J.L., and Nicewander, W.A. (1988). Thirteen ways to look at the correlation coefficient. *Am. Statistician* 42, 59–66.
111. Treuner-Lange, A., and Søgaard-Andersen, L. (2014). Regulation of cell polarity in bacteria. *J. Cell Biol.* 206, 7–17.
112. Dworkin, J. (2009). Cellular polarity in prokaryotic organisms. *Cold Spring Harbor Perspect. Biol.* 1, a003368.
113. Duddu, A.S., Majumdar, S.S., Sahoo, S., Jhunjhunwala, S., and Jolly, M.K. (2022). Emergent dynamics of a three-node regulatory network explain phenotypic switching and heterogeneity: a case study of Th1/Th2/Th17 cell differentiation. *Mol. Biol. Cell* 33, ar46.
114. Ghaemmaghami, S., Huh, W.-K., Bower, K., Howson, R.W., Belle, A., Dephoure, N., O’Shea, E.K., and Weissman, J.S. (2003). Global analysis of protein expression in yeast. *Nature* 425, 737–741.
115. Huh, W.-K., Falvo, J.V., Gerke, L.C., Carroll, A.S., Howson, R.W., Weissman, J.S., and O’Shea, E.K. (2003). Global analysis of protein localization in budding yeast. *Nature* 425, 686–691.
116. Heim, R., Prasher, D.C., and Tsien, R.Y. (1994). Wavelength mutations and posttranslational autoxidation of green fluorescent protein. *Proc. Natl. Acad. Sci. USA* 91, 12501–12504.
117. Zhang, G., Gurtu, V., and Kain, S.R. (1996). An enhanced green fluorescent protein allows sensitive detection of gene transfer in mammalian cells. *Biochem. Biophys. Res. Commun.* 227, 707–711.
118. Lee, S., Lim, W.A., and Thorn, K.S. (2013). Improved blue, green, and red fluorescent protein tagging vectors for *S. cerevisiae*. *PLoS One* 8, e67902.
119. Shaner, N.C., Steinbach, P.A., and Tsien, R.Y. (2005). A guide to choosing fluorescent proteins. *Nat. Methods* 2, 905–909.
120. Merzlyak, E.M., Goedhart, J., Shcherbo, D., Bulina, M.E., Shcheglov, A.S., Fradkov, A.F., Gaintzeva, A., Lukyanov, K.A., Lukyanov, S., Gadella, T.W.J., and Chudakov, D.M. (2007). Bright monomeric red fluorescent protein with an extended fluorescence lifetime. *Nat. Methods* 4, 555–557.
121. Papagiannakis, A., Niebel, B., Wit, E.C., and Heinemann, M. (2017). Autonomous metabolic oscillations robustly gate the early and late cell cycle. *Mol. Cell* 65, 285–295.

## STAR★METHODS

### KEY RESOURCE STABLE

REAGENT or RESOURCE	SOURCE	IDENTIFIER
<b>Bacterial and virus strains</b>		
pFA6a-link-yomCherry-CaURA3	Addgene	Cat#: 44876
<b>Chemicals, peptides, and recombinant proteins</b>		
Pheromone (alpha factor peptide hormone)	GenScript	Cas: 59401-28-4
50× TAE buffer	Solarbio	Cat#: T1060-500
Lithium acetate	Aladdin	CAS: 546-89-4
SYBR™ Safe DNA Gel Stain	Invitrogen	Cat#: S33102
Polyethylene Glycol	Aladdin	Cat#: P103728
<b>Experimental models: Organisms/strains</b>		
<i>Saccharomyces cerevisiae</i> : S288C	SGD	ATCC 201388
<b>Oligonucleotides</b>		
ssDNA	sigma	Lot#: SLBX8964
homologous long arms F'	This paper	N/A
homologous long arms R'	This paper	N/A
Primers: Confirming insertion of the gene fragment downstream of <i>FUS3</i> . Forward: AAGTCGCTTCCCATGTACCC	This paper	N/A
Primers: Confirming insertion of the gene fragment downstream of <i>FUS3</i> . Backward: GTTGCGTAACTGCTCCCTT	This paper	N/A
6aa [GS]x linker: ggtagcggcagcggtagc	This paper	N/A
<b>Software and algorithms</b>		
MATLAB	MathWorks	<a href="https://www.mathworks.com/products/matlab.html">https://www.mathworks.com/products/matlab.html</a>
CellASIC™ ONIX	CellASIC	N/A
NIS-Elements	Nikon	N/A

## RESOURCE AVAILABILITY

### Lead contact

Further information and requests should be directed to and will be fulfilled by the lead contact, Jin Wang ([jin.wang.1@stonybrook.edu](mailto:jin.wang.1@stonybrook.edu)).

### Materials availability

This study did not generate new materials.

### Data and code availability

- All data reported in this paper will be shared by the [lead contact](#) upon reasonable request.
- This study did not generate new code. Any additional information required to reanalyze the data reported in this paper is available from the [lead contact](#) upon request.
- Any additional information required to reanalyze the data reported in this paper is available from the [lead contact](#) upon request.

## EXPERIMENTAL MODEL AND SUBJECT DETAILS

### Yeast strain

The budding yeast *Saccharomyces cerevisiae* strain S288C (ATCC 201388: *MATa his3Δ1 leu2Δ0 met15Δ0 ura3Δ0*) was used in this study.<sup>114,115</sup> The key experimental strain was a *FUS3*-GFP fusion strain, where green fluorescent protein (GFP) was fused to the C-terminus of the *FUS3* gene (Systematic Name: YBL016W) to generate a *FUS3*-GFP fusion protein. This fusion strain originated from the Yeast GFP Fusion Localization Database initially constructed by the O'Shea and Weissman labs at UC San Francisco to systematically analyze protein localization

in budding yeast and currently hosted by SGD. The database covers over 6000 *S. cerevisiae* strains based on the S288C background. This strain has auxotrophic markers including deletions of *HIS3* and other genes involved in amino acid biosynthesis, resulting in nutritional deficiencies and auxotrophy. In the *FUS3*-GFP fusion strain, the MAP kinase Fus3 is fluorescently labeled with GFP, enabling real-time tracking of Fus3 in live cells. We selected this strain due to its representativeness and the controllability of genetic manipulation.

## METHOD DETAILS

### Preparation of pheromone culture medium

The chosen stimulant for our experiments was a peptide hormone called pheromone, specifically an  $\alpha$ -factor peptide hormone with a molecular weight of 1683.98 and a molecular formula of  $C_{82}H_{114}N_{20}O_{17}S$ . The  $\alpha$ -factor pheromone arrests a-type yeast cells in the G1 phase of their cell cycle, induces the expression of mating genes, and guides cell growth toward mating partners. The pheromone peptide powder used in our study was sourced from GenScript (10 mg, purity >95%).

Different concentrations of pheromone were prepared as follows: Initially, a specified quantity of the pheromone peptide powder was weighed and dissolved in liquid culture medium YPD (Yeast extract 10 g/L, Peptone 20 g/L, Dextrose 20 g/L, Agar 10 g/L) or YNB (Yeast Nitrogen Base Without Amino Acids 6.8 g/L, Dextrose 5 g/L, Uracil 76 mg/L, 50 $\times$  MEM Amino Acids 20 mL/L) to create a 1000  $\mu$ M stock solution of pheromone culture medium, which was stored at  $-80^{\circ}\text{C}$  or  $-20^{\circ}\text{C}$ . Before the initiation of microscopic observation experiments, the pheromone culture medium was serially diluted to the desired experimental concentrations within a clean bench. It's important to note that while solid pheromone powder is commonly stored at  $-20^{\circ}\text{C}$ , pheromone culture medium prepared using YPD or YNB as solvents should be stored for a limited duration to prevent degradation and accuracy discrepancies.

### Flow cytometry analysis

To determine the critical concentration of pheromone, we employed flow cytometry as a preliminary screening method. Yeast cells were cultured in YPD medium with varying pheromone concentrations (0.01  $\mu$ M, 0.05  $\mu$ M, 0.1  $\mu$ M, 0.2  $\mu$ M, 0.4  $\mu$ M, 0.6  $\mu$ M, 1.0  $\mu$ M, 1.5  $\mu$ M) for 24 h. The yeast cells were cultured in a shaker at 250 rpm and  $30^{\circ}\text{C}$  to ensure consistent growth conditions throughout the experiment. After incubation, 105,000 yeast cells were collected from each sample for subsequent analysis. The flow cytometry analysis was performed using a BD Accuri C6 Flow Cytometer to measure the fluorescence intensity of *FUS3*-GFP and the cell size. The flow cytometry measurements were performed using the FL1-A channel, which represents the fluorescence intensity of cells following excitation at 488 nm. The resulting data were analyzed by fitting the fluorescence intensity histograms using a Gaussian function with two peaks. The parameters of the fitted curves were determined using the nonlinear least squares method (nlinfit) in MATLAB. The fitted curves were then plotted along with the original histogram to visualize the distribution of fluorescence intensities. The x axis represents the logarithmic scale (base 10) of fluorescence intensity, showing the range of intensity values. By taking the logarithm, the data with a wide range of scales were transformed into a more easily comparable and interpretable linear scale. On the other hand, the y axis represents the probability density distribution. In our calculations, we utilized the "hist" function, a data analysis tool in MATLAB, to compute the histogram of the data. The parameter "n" corresponds to the frequency (or frequency count) of each histogram bin. By dividing the frequency count by the total sample size of 105,000, the frequency was converted to probability density. Therefore, the y axis represents the probability density distribution of each histogram bin, reflecting the relative frequency of corresponding intensity values. The resulting bar plots depict the distribution of cell scattering signal intensity under different pheromone concentrations.

The 3D top view of the probability density distribution illustrates the base-10 logarithmic transformation of FSC-A on the x axis and the logarithmic transformation of SSC-A on the y axis. These parameters are commonly used in flow cytometry. FSC-A (Forward Scatter-Angle) measures the intensity of light scattered at a forward angle, which reflects the size and complexity of cells or particles. Typically, larger or more complex cells exhibit higher forward scatter intensity, enabling estimation of cell size or particle complexity. SSC-A (Side Scatter-Angle) captures the intensity of light scattered at a side angle, providing insights into the internal structure and complexity of cells. The measurement of SSC-A is influenced by the scattering properties of cellular components and particles, facilitating evaluation of cell morphology, particle complexity, and cell viability.

### Microfluidic platform for yeast cell cultivation and operational procedure

For the cultivation of yeast cells, we employed the CellASIC ONIX Y04C-02 microfluidic platform designed by CellASIC. This platform, coupled with the CellASIC ONIX microfluidic temperature control system, offers temperature-controlled and dynamically controllable micro-environments for yeast cells. The platform consists of four independent well units labeled A to D, each containing six sample wells (e.g., A1-A6) for introducing media or drugs, one waste well (e.g., A7) for collecting waste, and one inoculation well (e.g., A8) for introducing yeast cells (Figure S16). Each well unit has capture regions with three different heights: 3.5  $\mu$ m, 4.0  $\mu$ m, and 4.5  $\mu$ m, allowing long-term confinement of cells in a specific region.

Our specific operational procedure is as follows: First, we adjusted the temperature for yeast cell cultivation to  $30^{\circ}\text{C}$ . Then, we introduced the yeast cells into the microfluidic platform through the inoculation well (A8) using a programmed flow rate of 5 psi (pounds per square inch) for 5 s. Next, we incubated the yeast cells in the microfluidic environment with regular YNB medium at a flow rate of 1 psi for 1 h in well A2 to facilitate their adaptation. Subsequently, we cultured the yeast cells in YNB medium containing a specific concentration of pheromone at a

flow rate of 1 psi for 15 h in well A3. Finally, in well A4, which has the same concentration of pheromone as well A3, we continued culturing the yeast cells at a flow rate of 1 psi for an additional 20 h.

### Microscopy measurements

The fluorescence values of the single cells were measured using an inverted fluorescence microscopy (Ti-E, Nikon) with automated stage and focus, equipped with a high NA oil-immersion objective (1.45NA, 100 $\times$ ). We applied 488 nm laser and set the output power at 30mW (only 10% of the laser beam into the microscope objective), the fluorescence signals were collected by a cooled EM-CCD camera (897U, Andor). All images were acquired using both bright field imaging and fluorescent field imaging. These images were acquired by Nikon software. Data analysis were accomplished through a combination of manual and automated analysis using custom MATLAB code. Many trajectories were taken from a time-lapse microscopy. The fluorescent images were periodically captured and recorded every 10 min. The fluorescent data of each cell at each time point were collected for the following discussion.

### Basis of fluorescent protein and interval choices

GFP (S65T) is a variant of green fluorescent protein (GFP) containing a serine to threonine mutation at position 65. This mutation results in faster chromophore maturation compared to wild type GFP. The maturation half-life of GFP (S65T) is around 10–15 min at 37°C.<sup>116,117</sup> In contrast, wild type GFP has a longer maturation half-life of 25–30 min at 37°C.<sup>116</sup> The faster maturation of GFP (S65T) makes it better suited for studying dynamic processes in living cells.<sup>115</sup> The mCherry is a red fluorescent protein optimized from mRFP1 derived from the coral *Discosoma* sp. yomCherry is a yeast-optimized variant of mCherry.<sup>118</sup> At 37°C, the maturation half-life of mCherry is around 15 min.<sup>119</sup> Some studies have reported a maturation time of around 20 min for mCherry,<sup>118</sup> likely due to subtle differences in experimental conditions. This is faster than wild type GFP but may be different for yomCherry due to codon optimization and other factors affecting protein folding in yeast. The A206K mutation can further accelerate the maturation of mCherry to around 5 min at 37°C.<sup>120</sup>

In this study, we chose GFP (S65T) and mCherry (yomCherry) as the fluorescent tags. Based on previous reports, the maturation half-lives of GFP (S65T) and mCherry at 37°C are around 10–15 min<sup>116,117</sup> and 15 min,<sup>119</sup> respectively. Considering that the maturation kinetics of both fluorescent proteins are on the order of 5-fold multiples of minutes, and to ensure that sufficient fluorescent proteins have matured between image acquisitions, we selected a time interval of 10 min between frames for time-lapse microscopy imaging experiments. This imaging interval ensures that newly synthesized GFP (S65T) and mCherry/yomCherry fusion proteins can complete maturation and become fluorescent before the next image is acquired. Thereby, we can visualize the real-time dynamics and capture biologically meaningful events without being limited by the fluorescent protein maturation kinetics. The 10 min interval provides a reasonable balance between capturing rapid dynamic processes, allowing fluorescent protein maturation, and minimizing photobleaching over long-term imaging. Specifically, the 10 min interval allows detection of faster dynamics compared to longer intervals, provides sufficient maturation time based on the half-lives of GFP and mCherry, acquires higher temporal resolution data, and was verified experimentally to show no artifacts of immature fluorescence.

### Background signal processing

In our study, we acknowledge the presence of background signal in the fluorescence imaging, with an intensity range of 90–182. However, we would like to emphasize that the measured average fluorescence signal intensity within the cell nucleus was 13000 at the non-equilibrium steady state, while the fluorescence intensity outside the nucleus was measured as 5400. Given the substantial difference in magnitude between the fluorescence signal and background signal, we carefully evaluated the impact of the background signal on our fluorescence measurements. After thorough consideration, we concluded that the influence of the background signal on the fluorescence signal is minimal and can be disregarded in our analysis. Therefore, we made the decision not to employ a specific background subtraction method.

It is important to note that our decision was based on the significant difference in intensity levels between the fluorescence signal and background signal, along with the experimental conditions under which our study was conducted. We took into account the specific characteristics of our samples and the fluorescence probe used, which contributed to the robustness and reliability of our measurements. While we acknowledge the potential for background signal variations over time, we conducted further analysis and confirmed that such variations have minimal impact on the correlation between nuclear and cytoplasmic fluorescence. Our data indicate that the observed correlation primarily arises from the localization of the target protein and the specificity of the fluorescent probe.

### Data collection and sample sizes

Our data collection involved the analysis of time-series sequences, where many independent samples were observed multiple times, resulting in a combination of hundreds of cells observed hundreds of times. For each pheromone concentration, the total number of cells in the time-series dataset is as follows (the total cell counts here refer to cells across all frames of the trajectories, from the first frame to the last frame): 0.7  $\mu$ M has 33,538 cells, 0.8  $\mu$ M has 29,614 cells, 1.0  $\mu$ M has 36,009 cells, 2.0  $\mu$ M has 50,277 cells, and 3.0  $\mu$ M has 27,067 cells. Additionally, the number of trajectories or single-cell observations for each concentration is as follows: 0.7  $\mu$ M has 207 trajectories, 0.8  $\mu$ M has 190 trajectories, 1.0  $\mu$ M has 221 trajectories, 2.0  $\mu$ M has 227 trajectories, and 3.0  $\mu$ M has 149 trajectories. Due to variations in the number of frames observed per trajectory, it is not possible to list them individually.

To provide a more accurate description, we want to highlight that the data analyzed at the steady state consists of the frames from the 60th frame of each trajectory to the final frame. At the steady state, the sample sizes for each pheromone concentration are as follows: 21,335 cells

at 0.7  $\mu\text{M}$ , 18,408 cells at 0.8  $\mu\text{M}$ , 23,041 cells at 1.0  $\mu\text{M}$ , 36,886 cells at 2.0  $\mu\text{M}$ , and 18,276 cells at 3.0  $\mu\text{M}$ . It's important to note that to minimize errors arising from differences in cell environment and individual variations, the observed yeast cells were cultured in identical media containing different pheromone concentrations.

### Estimation of uncertainty and interpretation of results

In order to estimate the uncertainty of our measurements, we employed the bootstrap resampling method. The original dataset, denoted as "tra", consisted of "k" trajectories. We performed "num\_bootstraps" iterations to generate bootstrapped samples for analysis. For each iteration, we created a bootstrapped sample by randomly sampling, with replacement, a subset of the original dataset for each trajectory. We ensured that the length of each bootstrapped sample was at least 60 frames, as this was our minimum requirement for analysis. The inner intensity values of the selected frames were extracted from each trajectory and stored in the "bootstrapped\_sample" variable.

Next, we analyzed the bootstrapped samples by calculating the mean inner intensity value for each sample. To account for variations in sample size, we calculated the sum of the inner intensity values and the total length of the bootstrapped sample. The mean was then computed as the sum divided by the total length. By repeating this process for "num\_bootstraps" iterations, we obtained a distribution of mean inner intensity values. From this distribution, we computed the 95% confidence interval using the `prctile` function, with percentiles set to [2.5, 97.5]. This confidence interval provides a range within which we can be 95% confident that the true population mean falls. Additionally, we calculated the standard error of the mean as the standard deviation of the bootstrapped results. This provides a measure of the precision of our estimates.

Based on our analysis, the calculated confidence interval, [CI<sub>1</sub>, CI<sub>2</sub>], represents the range within which we can be 95% confident that the true population mean inner intensity falls. The standard error, "standard\_error\_inner", provides an estimate of the variability of the mean estimates across different bootstrapped samples. It is important to note that the validity of our results relies on the assumption that the bootstrap samples accurately represent the underlying population. The robustness and reliability of our findings are supported by the large number of bootstraps performed (num\_bootstraps = 1000) and the careful selection of frames for analysis (Table S4).

### Dual fluorescence system construction

The yeast strain used in this experiment is *Saccharomyces cerevisiae* S288C (ATCC 201388: MATahis3 $\Delta$ 1 leu2 $\Delta$ 0 met15 $\Delta$ 0 ura3 $\Delta$ 0).<sup>114,115</sup> For constructing the dual-color strains, we employed the strain YAL041W (CDC24-GFP) from the Huh et al. Yeast GFP collection as the parental strain for our gene editing. To create the *FUS3*-yomCherry strains, we performed gene editing on YAL041W strain. According to Huh et al., the yeast strains with chromosomally GFP-tagged ORFs were constructed using *his3 $\Delta$*  auxotrophic selection. Therefore, for strain construction, we employed a similar approach, using uracil-deficient (*URA3 $\Delta$* ) medium for selection for constructing yeast strains with chromosomally RFP-tagged ORFs.

Before gene editing of *FUS3*, we designed the recombinant vector by referencing the sequence of the plasmid "pFA6a-link-yomCherry-CaURA3".<sup>118</sup> The core sequence "yomCherry-CaURA3" from this plasmid was integrated into the homologous recombination target fragment that we designed (Figure S17). The recombinant vector consists of the left and right homology arms (F/R) of the *FUS3* gene, a flexible chain (linker) connecting *FUS3* and the red fluorescent gene (yomCherry), and a screening gene (CaURA3) that compensates for uracil deficiency-induced lethality in yeast. To create the homologous arms (F/R) within the *FUS3* sequence, we selected 300 bp regions before and after the stop codon (TAG) of the *FUS3* gene as the left and right homologous long arms (F'/R'). Next, we chose a flexible chain (6aa [GS]x linker) to act as a structural buffer, ensuring the proper fusion of the red fluorescent reporter gene (yomCherry) to the 3' end of the *FUS3* gene without disrupting the protein structure between the two groups. The final recombinant vector containing "yomCherry-CaURA3" was then introduced into yeast cells.

The designed DNA sequence was synthesized by Shanghai Biotech and ligated into the plasmid "pUC57". The purified target plasmid was used as a template for PCR cloning. PCR amplification of the target fragment was performed using "TransStart FastPfu Fly DNA Polymerase" (TaKaRa). Purified PCR products were used as templates for further cloning (Table S5). The yeast strains "CDC24-GFP" were transformed with the "*FUS3*-yomCherry" fragments using the lithium acetate method. Yeast transformants were screened on URA-deficient solid media (YPD supplemented with 5-fluoroorotic acid) and incubated at 30°C for 3–5 days. Genomic DNA was extracted using the "GeneJET Genomic DNA Purification Kit" (Thermo). Colony PCR was performed using GFP-specific and gene-specific primers to confirm the insertion of the "*FUS3*-yomCherry" fragment. After purification using the "GeneJET Gel Extraction Kit" (Thermo), the successful PCR products were subjected to sequencing for final validation.

### Quantifying fluorescent tag photobleaching

Due to the continuous uptake of energy from the environment, gene expression levels within cells are subject to fluctuations. It is crucial to ensure that the gene of interest can achieve stable expression within a controlled range when quantifying photobleaching rates. In this study, we selected the *CDC28*-GFP-*SIC1*-yomCherry strain as our experimental model, with both *Cdc28* and *Sic1* being cell cycle-related proteins. The controlled condition we chose was the yeast cell's own cell cycle. To maximize the resemblance to the actual experimental conditions, we employed the same microscope illumination settings used for capturing the fluorescence intensities of *Fus3* and *Cdc24* when exciting the fluorescence proteins (GFP and yomCherry). The same microfluidic media conditions were applied except without alpha-factor induction. Due to continuous budding, the observation period for each cell under the microscope was limited by available space. In total, we collected single cell data for 92 cells, with each cell observed for approximately 1340 min.

By recording the bud emergence time points, the fluorescence intensity time course data was divided into segments, with each segment representing one cell cycle. The first segment was chosen from bud point 1 to bud point 2, as the data from 0 to bud point 1 may not constitute a full cycle. The last segment was chosen similarly between the final two bud points. We extracted the expression trajectories of Cdc28 and Sic1 for each full cell cycle segment, calculated the mean intensity for each segment, and thereby converted the trajectories into discrete points. Finally, we computed the non-zero average trajectory across the 92 cells according to time order as the final time course data representing cellular expression levels. The exponential decay function used to model the photobleaching of CDC28-GFP and SIC1-yomCherry can be represented as follows. For CDC28-GFP,

$$\text{For SIC1-yomCherry: } F(t) = F(0) \bullet e^{-\lambda_1 \bullet t}.$$

$$F(t) = F(0) \bullet e^{-\lambda_2 \bullet t}.$$

Where  $F(t)$  is the fluorescence intensity at time  $t$ .  $F(0)$  is the initial fluorescence intensity at  $t = 0$ .  $\lambda_1$  represents the photobleaching rate of CDC28-GFP in units of per 10 min ( $\text{min}^{-1}$ ).  $\lambda_2$  represents the photobleaching rate of SIC1-yomCherry in units of per 10 min ( $\text{min}^{-1}$ ).  $\lambda_1 = 0.02415$  per 10 min,  $\lambda_2 = 0.015358$  per 10 min for SIC1-yomCherry. These quantified rates suggest that photobleaching is still within a reasonable range after 1340 min, and its effects on the experimental results can be initially ignored.

### Real time image analysis

Bright-field images obtained using widefield fluorescence microscopy with total internal reflection (TIRF) capabilities were segmented, aligned, and labeled using a custom MATLAB routine. We segmented the cells according to bright field images to obtain the outlines of the individual cells, and assigned each cell accordingly. Then we can collect the trajectories of the generations by the assigned id when the cells grow and divide, and obtain cell lineages. All the cell boundaries of yeast were manually corrected. The cell nuclei were distinguished by contouring the fluorescence images. Fluorescence intensity is the average of all fluorescence intensity within the cell boundary. The real-time trajectories were obtained by automatic tracking, based on the cell overlaps between the adjacent frames. All trajectories require manual correction.

### Steady-state image analysis

In order to explore the underlying mechanism of the bimodality, we collected the real time fluorescence intensity trajectories (Figures 3A, S4, and S5), which show that the yeast response is in a steady state after about 600 min. This state means that the fluorescence intensity of the yeast inside and outside the nucleus does not increase or decrease significantly. The histograms of inner and outer fluorescence intensity were obtained by the steady-state fluorescence trajectories (Figures 3B and S6–S8). The shape characteristics of the yeast are described by the  $H_n$  in the yeast. The growth rate of the yeast is the numerical differentiation of the  $H_n$ . All the trajectories can be used to provide the quantitative analysis through Hidden Markov Chain Model (HMM). During the HMM fitting, the parameters of the fluorescence state were fixed. The distribution of high fluorescence state and low fluorescence state in two growth rates can be obtained by counting the state points on the trajectories.

### Cell fate identification using Hidden Markov Model

We employed a Hidden Markov Chain Model (HMM) to fit the time trajectories of cell morphology. HMM is a probabilistic model that estimates unknown hidden states (cell fate categories) based on observed data (time trajectories of cell morphology). In this context, the hidden states represent different cell morphologies or states, while the observed data comprises the time trajectories of cell morphology. During the exploratory analysis, we observed multiple peaks in the histogram plot of cell morphology, suggesting the presence of distinct cell fate categories. The number and distribution of peaks provided an initial estimate of the potential different cell fate categories. These peaks likely corresponded to various cell states or morphologies. We initialized the HMM model by specifying the number of hidden states (representing the presumed different cell fate categories) and setting initial parameters. These initial parameters could include transition probabilities between hidden states and probability distributions corresponding to each state. Next, we fed the time trajectories into the HMM model, allowing the model to estimate the probabilities of cells being in different morphology states at each time point. We used the Baum-Welch algorithm to iteratively optimize the HMM model's parameters, aligning the model's fit with the observed data. This iterative process involved adjusting the model's parameters to enhance its explanatory power concerning the known data. To ensure finding the global optimum, we performed multiple iterations of the HMM analysis, each time using different random initial parameters. After several iterations, the HMM model outputs the probabilities of cells being in different morphology states at each time point. Using these probabilities and applying certain thresholds or criteria, we categorized the cell morphologies into distinct cell fate states. For instance, we determined the time points with higher probabilities of specific cell morphology states, thus assigning them to corresponding fate categories. Overall, our goal was to fit the time trajectories of cell morphology using the HMM model and classify cell fate based on the model's probability outputs. This approach enables us to understand cell behavior in different states and investigate the underlying mechanisms of cell state transitions.

### Distinguishing the boundaries of the nucleus

When yeast cells are stimulated by pheromones, two responses occur: first, the cell cycle is arrested in the G1 phase, and second, mating-related genes are activated. To ensure both responses, large amounts of Fus3 are delivered to the nucleus, causing Fus3 to form fluorescent clusters in the nucleus.<sup>27–35</sup> Previous articles have employed the fluorescent cluster region as the nucleus.<sup>51,55,121</sup> When we observed cell budding and division under the microscope, the fluorescence clusters split in half, which corresponds to the separation of the daughter cell's nucleus from the mother cell's nucleus, indicating that it is feasible to use the fluorescence cluster as the nucleus. We use an algorithm similar to contour lines to divide each pixel in a cell into four distinct calculation levels. Then, the fluorescent spots at the same contour level are joined into closed regions. By comparing each level individually, it was determined that the outer edge of the highest level, which serves as the boundary between the nucleus and the cytoplasm, is best able to encompass intracellular fluorescent clusters (Figure S18). Therefore, we propose that fluorescence above this threshold is localized within the nucleus, whereas fluorescence below this threshold is localized outside of the nucleus.

### Filled circle model in cell shape

After identifying the boundary of the cell shape with "MATLAB", we filled it in with circles along the cell's long axis in turns, with the area of the circle filled in each time being guaranteed to be the largest area of the remaining unfilled part. To ensure the accuracy of the cell morphology ( $H_n$ ) at various stages, we set a minimum circle diameter (5 pixels) to avoid significantly increasing the shape's internal gap.

### Characterizing the deformation behavior of yeast cells

To quantify the behavior of yeast cells of which deformation rate did not vary uniformly over time, we characterized various cell components using a circular fill pattern (Figure 5A). The largest circle represents the initial main part of the cell, while the smallest circle represents the newly formed portion at the top of the cell. For example, there are two filled circles denoted by the letters  $R_0$  and  $R_1$  within the yeast cell.  $R_0$  is the larger of the two circles, whereas  $R_1$  is the smaller (Figure S19). If the filled circle  $R_1$  of the cells grows uniformly in size from small to large (model-1: " $R_{1_1} \rightarrow R_{1_2} \rightarrow R_{1_3} \rightarrow R_{1_4}$ "), then the ratios of the smallest circle to the largest circle in the cell will be uniformly distributed. If, on the other hand, the cell grows as in model-2 (" $R_{1_1} \rightarrow R_{1_2} \rightarrow R_{1_3} \rightarrow R_{1_3} \rightarrow R_{1_4}$ ") with the growth temporarily halted at  $R_{1_3}$ , then  $R_{1_3}$  will be observed repeatedly, increasing the probability of the  $R_{1_3}/R_0$ . When the size ratio of the smallest and largest circles was used as an observable value, we noticed that the statistical result was mostly around 0.27 at 0.7  $\mu\text{M}$  (Figure S13). This clearly demonstrated that when the size ratio was 0.27, the cell was growing more slowly or was temporarily not growing, and thus there were more opportunities to observe this ratio distribution during cell polar growth. That is, the rate of deformation or the capacity for growth at various locations within a cell were not exactly identical.

To quantify the various cell deformations that occur during cell growth, we considered a value ( $H_n$ ) comparable to the harmonic mean to characterize the cell morphology, i.e.,  $H_n = n \left( \frac{1}{R_1} + \frac{1}{R_2} + \dots + \frac{1}{R_n} \right)$ . The significant advantage of  $H_n$  is that it is particularly sensitive to small morphological changes at various locations of the cell. For example, we set the radius of the filled circle in the cell as  $R_1$ ,  $R_2$ , and  $R_3$  in advance. If the cell grew longitudinally (in length), a new filled circle ( $R_4$ ) was added to the cell; consequently, the value of  $H_n$  increased as the number of elements in parentheses increased from three to four. In contrast, as cells expanded laterally (in width), the values of  $H_n$  decreased regardless of whether the filled circle's radius increased.

### Derivation of the transition rates

The master equation can be written as

$$\frac{d}{dt} \begin{pmatrix} P_1 \\ P_2 \end{pmatrix} = \begin{pmatrix} k_{11} & k_{12} \\ k_{21} & k_{22} \end{pmatrix} \begin{pmatrix} P_1 \\ P_2 \end{pmatrix} = \begin{pmatrix} -a & b \\ a & -b \end{pmatrix} \begin{pmatrix} P_1 \\ P_2 \end{pmatrix}.$$

Here  $P_1$  and  $P_2$  are the probabilities of the low expression state and high expression state, respectively, while  $k_{ij}$  ( $i, j = 1, 2$ ) is the transition rate from  $P_i$  to  $P_j$ . We can write down the solution as follows with the initial conditions  $P_1(0) = 1$ ,  $P_2(0) = 0$ ,

$$P_1(t) = \frac{b+ae^{-(a+b)t}}{a+b}; P_2(t) = -\frac{a(-1+e^{-(a+b)t})}{a+b}.$$

Then the transition probability between the low expression state and the low expression state is  $P_{11} = P_1(\delta t) = \frac{b+ae^{-(a+b)\delta t}}{a+b}$ , where  $\delta t$  is the observational time window for each time, here  $\delta t = 10 \text{ min}$ . With the initial conditions  $P_1(0) = 0$ ,  $P_2(0) = 1$ ,

$$P_1(t) = -\frac{b(-1+e^{-(a+b)t})}{a+b}; P_2(t) = \frac{a+be^{-(a+b)t}}{a+b}.$$

Then the transition probability between the high expression state and the high expression state is  $P_{22} = P_2(\delta t) = \frac{a+be^{-(a+b)\delta t}}{a+b}$ , where  $\delta t$  is the observation time window for each time, here  $\delta t = 10 \text{ min}$ .

According to the HMM analysis, when the pheromone dose is 0.7  $\mu\text{M}$ , the transition matrix is  $P = \begin{pmatrix} P_{11} & P_{12} \\ P_{21} & P_{22} \end{pmatrix} = \begin{pmatrix} 0.6900 & 0.3100 \\ 0.3711 & 0.6289 \end{pmatrix}$ . So we can get the transition rate as:  $a = 0.052017$  (1/min),  $b = 0.062270$  (1/min).

### Calculating residence and switching times in multi-stable systems

To calculate the residence time of multi-stability, we first employ a Markov model to fit the real-time trajectory data, allowing us to discern the states to which the data points belong at different time points. Subsequently, we systematically analyze various indicators for each trajectory during the non-equilibrium steady state period (from the 60th frame until the last frame). These indicators include the number of occurrences of different fates and the number of regions associated (or the number of state changes) with different fates. The division of regions for different fates is defined as follows: continuous segments of identical fates are considered as one region, and isolated individual occurrences of a fate are also counted as separate regions. Having obtained the relevant statistics for each trajectory, we aggregate the counts of the same fates across all trajectories. This cumulative count is then divided by the total count of regions for the same fates across all trajectories. The resulting quotient is multiplied by the interval between consecutive image frames taken by the microscope. The outcome of this calculation represents the average residence time of cells in various fates. By employing this rigorous statistical approach, we gain insights into the dynamics of multi-stability in our system, capturing the average duration that cells spend in specific fates under the influence of pheromone concentrations.

To quantify the temporal dynamics of cellular state transitions within our multi-stability framework, we employ a systematic approach akin to our residence time calculation. Iterating through each pair of states (state\_from and state\_to) while excluding self-transitions, we quantify the number of switches from state\_from to state\_to using the num\_switches array. Simultaneously, we track the number of continuous occurrences of state\_from leading to the transition to state\_to, recorded in the num\_continuous\_states array. Subsequently, the total number of switches (total\_switches) across all trajectories is computed, and if transitions are present (total\_switches > 0), the average number of continuous states preceding each switch is calculated. This average is multiplied by the microscope interval to estimate the average switching time. The resulting switching times are aggregated in a transition matrix, offering a quantitative depiction of temporal transitions between different states.

### The statistical physics connection between cell state switching and residence time

In physics, the cell state switching time between initial and target state is equal to the residence times of the starting state in two state systems. In other words, the switching time is equal to the waiting time for the switching to occur in this case. The cell fates and the associated decisions involve states and the transitions between distinct phenotypic states, which emerge from the underlying interactions leading to the formation of the landscape. Specifically, the kinetic transition rates between different cell states often depend on the potential barriers separating them. The cells prefer to stay in the valleys of the landscape, corresponding to the phenotypic steady states. The depth of the valley often determines the stability of the associated steady state. Quantitatively, the mean residence time of a state is the same as the inverse of the transition rate escaping that state for the two states system. In other words, the lower the transition rate out of a steady state due to high potential barriers, the longer the average residence time in that state will be before switching. Therefore, residence times provide a meaningful quantification of the relative stability. However, when the number of states is three or more, there is no direct and simple relationship between residence time and switching time. The switching time depends not only on the barrier heights but also on all the possible channels available from the initial state to the other states it can escape to.

From this statistical physics perspective, the emergent multi-stability in biological systems is rooted in the inherent underlying interactions, giving rise to the emergence of the landscape topography endowed by the relative stability of the steady states. This relative stability is quantified by the residence times extracted from real-time experimental traces. The kinetic transition rates between different states also depend on the potential barriers separating them, ultimately contributing to the observed multistage dynamics. Importantly, the residence time serves as a crucial metric bridging experimental observations and theoretical models, providing a statistically meaningful measure to characterize the stability of distinct states. The extracted residence times, alongside the transition rates, offer valuable experimental validation for the predicted multi-stability on the non-equilibrium landscape originated from the inherent interactions.

### Unraveling the interplay of duration, pheromone concentration, and cell state switching

In our microscopic observations of yeast cells responding to pheromone, we discovered roughly a linear correlation between pheromone concentration and the prolonged duration of cell-cycle arrest. By statistically analyzing the average time yeast cells were arrested in G1 phase under different concentrations (Figure S3), we observed that the duration increased progressively with higher pheromone concentrations (except 3.0  $\mu\text{M}$ ). We note that the 3.0  $\mu\text{M}$  data point is inaccurate due to our inability to capture the specific budding recovery nodes during observations. This was partly due to overlooking the need to monitor budding recovery, and partly due to the limited liquid volume in the microfluidic device. To further quantify the correlation, we calculated a Pearson coefficient of 0.8194 between duration and concentration (Figure S14), indicating a highly positive relationship.

To elucidate the relationship between cell state switching and concentration as well as duration, we analyzed the residence times of multi-stability or cell state switching under different pheromone concentrations and durations (Tables S6, S7, and S8). From physics perspective, the emergence of cell state and associated state switching from one to another originates from the underlying interactions among the genes, which give rise to distinct stable states with different associated residence times, which collectively shaping the emergent landscape topography. Cell state switching time is closely related to the residence times of different steady states in two-state systems. The relative stability of the steady states is reflected in the residence times, with longer times indicating higher stability. In the bistability of Fus3, we described how the residence times of gene expression fates (or cell state switching) vary as a function of signal gradient and duration (Figure S15). We found the relationship between duration and cell state switching and that between concentration and switching. Different pheromone

concentrations as stimuli prolonged the G1 phase stall time of the cell cycle. Thus, the pheromone concentration can be seen as the cause, while the stall time and cell state switching are the consequences. However, when the number of states is three or more, there is no direct quantitative relationship between the residence time and switching time. The switching time depends not only on the barrier heights but also on all the channels between the initial state and other states it can escape to."

### Decomposing of the flux in the cell morphology

The kinetics of the cell morphological can be modeled by a four-state Markov process. The transition probability ( $M_{ij}$ ) can be calculated by counting the number of transitions in the state trajectories. Therefore, the master equation can be shown as follows:

$$\frac{dP_i}{dt} = \sum_j M_{ij}P_j \quad (\text{Equation 1})$$

Where  $P_i$  represents the probability of state  $i$ , and the transition probability  $M_{ij}$  represents the transition probability from state  $i$  to state  $j$ . For steady state, we set the left term of the master Equation 1 to zero, then we obtain the steady state solution  $P_i^S$ , which is the long time limit. The steady state flux between state  $i$  and  $j$  can be defined as:  $F_{ij} = -M_{ij}P_i^S + M_{ji}P_j^S$ . If the steady state of the system is in equilibrium state, the flux between any two nodes in the system is zero, that is the detailed balance condition. For the general biological system, it does not necessarily satisfy the detailed balance condition ( $F_{ij} \neq 0$ ), the system is in non-equilibrium steady state, there will be at least one net flux among states.

In order to study the non-equilibrium steady states, we can separate the dynamical process into two parts, one is the detailed balance part and the other is the detailed balance-breaking kinetic process. To describe the detailed balance breaking, we decompose the probability matrix. The component of the rate matrix  $MP$  can be decomposed into two parts, one being the symmetric matrix and the other cycle matrix, that is

$$MP = C + D \quad (\text{Equation 2})$$

Where  $D$  is the symmetric matrix  $D_{ij} = (M_{ij}P_i^S + M_{ji}P_j^S)/2$ ,  $C$  is the asymmetric matrix  $C_{ij} = (M_{ij}P_i^S - M_{ji}P_j^S)/2$ . Since the system contains four states, the asymmetric flux is not unique and contains three net cycle fluxes. Meanwhile, in order to ensure the consistency of decomposition for various pheromone concentration systems, the given base sets of flux decomposition were selected. Here, the base sets we selected are "State<sub>1</sub>-State<sub>2</sub>-State<sub>3</sub>-State<sub>4</sub>", "State<sub>1</sub>-State<sub>4</sub>-State<sub>3</sub>-State<sub>2</sub>", "State<sub>2</sub>-State<sub>4</sub>-State<sub>3</sub>-State<sub>2</sub>", the corresponding net fluxes are  $J_1$ ,  $J_2$  and  $J_3$ . The asymmetric matrix  $C$  can be rewritten as follows:

$$C = \begin{pmatrix} 0 & \frac{J_1}{2} & -\frac{J_2}{2} - \frac{J_1}{2} & \frac{J_2}{2} \\ -\frac{J_1}{2} & 0 & \frac{J_1}{2} - \frac{J_3}{2} & \frac{J_3}{2} \\ \frac{J_1}{2} + \frac{J_2}{2} & -\frac{J_1}{2} + \frac{J_3}{2} & 0 & -\frac{J_2}{2} - \frac{J_3}{2} \\ -\frac{J_2}{2} & -\frac{J_3}{2} & \frac{J_2}{2} + \frac{J_3}{2} & 0 \end{pmatrix}$$

The linear equations can be obtained by corresponding the numerical results of the above matrix  $C$  and the experimental statistics (Tables 5, 6, 7, 8, and 9). For example, three linearly independent parameters of  $C_{1,4}$ ,  $C_{1,3}$ ,  $C_{2,3}$  are selected for the linear equations originated from the underlying master equations.

The linear equations (0.7  $\mu\text{M}$ ) are  $\begin{pmatrix} C_{1,4} = \frac{J_2}{2} = 0.0036 \\ C_{1,3} = -\frac{J_2}{2} - \frac{J_1}{2} = -0.0067 \\ C_{2,3} = \frac{J_1}{2} - \frac{J_3}{2} = 0 \end{pmatrix}$ . Then, solving these linear equations one can get the net flux values of the non-equilibrium system.

### Gillespie algorithm-based simulation

To investigate the dynamics of the pheromone pathway and its impact on Fus3 expression level and cell morphology distribution in yeast cells, we employed the Gillespie algorithm to simulate the underlying biochemical reactions (Tables S1-S3). This algorithm allowed us to model the stochastic nature of the reactions and capture their temporal evolution. We constructed a simplified model of the pheromone pathway based on the functional and quantitative regulation obtained from databases such as KEGG, SGD, and EVEX, incorporating the known biochemical reactions involved in the pheromone signaling cascade and the feedback mechanisms associated with Fus3 expression. The reaction network consisted of species representing various molecular entities, with reaction rates defined based on available experimental data, kinetic constants, and literature information. Using the Gillespie algorithm, a stochastic simulation method, we simulated the time evolution of the reaction network, accounting for the discrete and probabilistic nature of the reactions.

The simulation procedure began with initialization, where the initial concentrations and simulation time were set to zero. Reaction rates were calculated based on species concentrations and kinetic constants. The total reaction rate was computed as the sum of individual rates. The next reaction was selected using a random number generator and propensity-based probabilities. Time was updated using the

exponential distribution and total reaction rate. The selected reaction was executed, leading to concentration updates. This entire process was iterated multiple times. Each iteration involved a cyclic execution of the aforementioned steps. The iterations continued until the desired simulation time was reached or the stopping criteria were satisfied. Throughout the simulation, we recorded Fus3 expression levels and monitored changes in cell morphology, determining expression levels by analyzing relevant species concentrations. This allowed us to characterize the distribution of Fus3 expression levels and correlate them with observed changes in cell morphology. By implementing the Gillespie algorithm and simulating the biochemical reactions of the pheromone pathway, we successfully determined the expression level of Fus3 and obtained insights into the distribution of cell morphology. This computational approach allowed us to study the dynamic behavior of the pheromone pathway and its impact on Fus3p regulation, as well as the calculation of cell morphology based on Bni1p concentration.

### The comprehensive description of the biochemical reactions in stochastic simulations

The biochemical reactions in our signal transduction model were derived from the preexisting gene regulatory network. These biochemical reactions include the processes of gene translation into the proteins, the phosphorylation of the proteins, the degradation of the proteins, the interaction between the proteins, and the transfer of the proteins within the nucleus and the cytoplasm of the cells. The following is an understanding of each chemical reaction (Table S3):

Reaction 1 depicts a portion of the gene *FUS3* being translated into a cytoplasmic protein at a certain rate. Reaction 2 depicts the gene *FUS3* generated by the indirect pheromone induction in addition to the known gene regulation. Reaction 3 is the reverse reaction of the reaction 2. Reaction 4 depicts the process of the phosphorylation of the protein produced by the gene *FUS3* induced by the pheromones outside the cell nucleus. Reaction 5 represents the gene *FUS3* produced by the self-activation of the phosphorylated protein Fus3 outside the cell nucleus. Reaction 6 is the reverse reaction of the reaction 5. Reaction 7 represents the process of the phosphorylation of a protein generated outside of the nucleus by the self-activating gene *FUS3*. Reaction 8 represents the transport of the phosphorylated Fus3 from the outside of the nucleus to the inside of the nucleus. Reaction 9 is the reverse reaction of the reaction 8.

Reactions 10 and 11 represent the degradation of the phosphorylated Fus3 both outside and inside the nucleus. Reaction 12 represents the translation of the gene *STE12* into the phosphorylated protein Ste12. Reaction 13 represents the impact of the gene *STE12* on the nuclear protein Fus3. Reaction 14 is the reverse reaction of the reaction 13. Reaction 15 represents the activation of the gene *STE12* by the nuclear Fus3. Reaction 16 represents the process of the translation of the gene *MSG5* into the phosphorylated protein Msg5. Reaction 17 represents the interaction between the phosphorylated protein Ste12 and the gene *MSG5*. Reaction 18 is the reverse reaction of the reaction 17. Reaction 19 represents the process of the translation of the gene *MSG5*, which is activated by the phosphorylated protein Ste12.

Reaction 20 represents the interaction between the phosphorylated protein *MSG5* and the gene *FUS3*. Reaction 21 is the reverse reaction of the reaction 20. The reaction 22 represents the inhibition of the gene *FUS3* expression by the phosphorylated protein *MSG5*. Reactions 23 and 24 represent the degradation of the proteins Ste12 and Msg5, respectively. Reaction 25 represents the process of the phosphorylation of protein Far1 generated by the gene *FAR1*. Reaction 26 represents the interaction between the Fus3 in the nucleus and the gene *FAR1*. Reaction 27 is the reverse reaction of reaction the 26. Reaction 28 represents the process of the transcription of the gene *FAR1*, regulated by the Fus3, into the protein. Reaction 29 represents the degradation of the protein Far1.

Reaction 30 represents the process of the gene *BNI1* generating the protein Bni1. Reaction 31 represents the interaction between the cytoplasmic Fus3 and the gene *BNI1*. Reaction 32 is the reverse reaction of the reaction 31. Reaction 33 represents the process of the indirect inhibition of the Fus3 expression outside of the nucleus by Bni1. Reaction 34 represents the interaction between the nuclear gene *BNI1* and the phosphorylated Far1. Reaction 35 is the reverse reaction of the reaction 34. Reaction 36 represents the process of the phosphorylated Far1-activated generation of the phosphorylated protein from the gene *BNI1*. Reaction 37 represents the interaction between the nuclear Fus3 and the gene *BNI1*. Reaction 38 is the reverse reaction of the reaction 37. Reaction 39 represents the process of the generation of phosphorylated protein from the gene *BNI1* activated by the phosphorylated Fus3 outside of the nucleus.

Reactions 40 and 41 denote the degradation of the phosphoproteins Bni1 both in the cytoplasmic and nuclear compartments.

### QUANTIFICATION AND STATISTICAL ANALYSIS

The fluorescence intensity of *FUS3*-GFP and cell size were quantified using a BD Accuri C6 flow cytometer. Microscopy images were processed and analyzed using MATLAB (Mathworks). Single-cell segmentation, tracking, and quantification of fluorescence intensity were performed using custom MATLAB scripts. Sample sizes and number of replicates are indicated in the corresponding figure legends. All graphs were generated using MATLAB. Statistical analyses were performed in MATLAB. Statistical significance was determined using Student's t-test, ANOVA, or non-parametric tests. p values are indicated by asterisks (\*p < 0.05, \*\*p < 0.01, \*\*\*p < 0.001). Error bars depict standard error of mean (SEM).